

# SPECTRAL ANATOMY OF QUANTUM GAUSSIAN PROCESS KERNELS

Jian Xu<sup>1,2,\*</sup>, Chao Li<sup>2</sup>, Guang Lin<sup>2</sup>, Yuning Qiu<sup>2</sup>, Delu Zeng<sup>3</sup>, John Paisley<sup>4</sup>, Qibin Zhao<sup>1</sup>

<sup>1</sup>RIKEN iTHEMS <sup>2</sup>RIKEN AIP <sup>3</sup>South China University of Technology <sup>4</sup>Columbia University

## ABSTRACT

Two recent results have reshaped quantum Gaussian processes (QGP). On the one hand, Lowe et al. (2025) rule out the exponential speedups claimed by HHL-based QGP regression in the typical, well-conditioned regime; on the other, an independent line of work shows that highly expressive quantum kernels suffer posterior pathologies that break Bayesian optimization. We show that these seemingly unrelated phenomena are governed by the same quantity: the normalized spectral entropy  $S(K)/\log n$  of the kernel Gram matrix. We prove a Cauchy–Schwarz tail bound on Nyström approximation error, a finite-sample variance-contraction identity in terms of Bach’s degrees of freedom  $d_\sigma(K)$ , and a characterization of the *target-dependent* optimal entropy via the intrinsic dimension of the target in the kernel eigenbasis. Empirically, the diagnostic is kernel-agnostic: hardware-efficient, matchgate, IQP and RBF/Matérn/RFF/deep-kernel families all collapse onto identical  $S/\log n$  curves on dequantization, ECE, and variance-contraction panels. The NLL sweet spot lives at high entropy for smooth targets and at low entropy for band-limited quantum-data targets. The diagnostic transfers from simulator to IBM Heron hardware with median absolute error 3.2% and mean 5.2% in  $S/\log n$  across 24 configurations at  $n_q = 4$ , with matchgate and IQP within 5% mean and a single HE configuration returning a 30% outlier that drops to 0.5% on rerun (attributed to calibration drift); the same diagnostic transfers to a second Heron backend (mean error 2.7%) and to a  $n_q = 6$  scale-up on the original backend (mean error 1.7%). No error mitigation is applied throughout.

## 1 INTRODUCTION

Quantum Gaussian processes (QGP) promise two things that classical GPs cannot easily deliver: kernels that encode physics-motivated symmetries (Jäger et al., 2026; Rapp & Roth, 2024), and—in principle—asymptotic runtime speedups for Bayesian inference via quantum linear solvers (Zhao et al., 2019c;a; Chen et al., 2022). The past eighteen months have however brought a sharp reframing.

First, Lowe et al. (2025) proved that the kernel matrices arising in many QGP regression settings—specifically, those for which HHL-based exponential speedups had previously been claimed—have condition number scaling  $\kappa(K) = \Omega(n)$ , so that the HHL pipeline delivers at most polynomial advantage in those regimes. Second, an independent line of work on quantum-kernel concentration (Thanasilp et al., 2024; Kübler et al., 2021) shows that highly expressive quantum feature maps produce kernel matrices that approach either the constant matrix  $c\mathbf{1}\mathbf{1}^\top$  or the identity  $I_n$ , causing the GP posterior to either over-fit confidently to garbage or collapse to the prior. Both pathologies destroy downstream uses of the posterior such as Bayesian optimization (Dai et al., 2023; Rapp & Roth, 2024).

Each finding has been treated as a separate cautionary tale. We argue they are the same tale, told from different angles. *The eigenspectrum of the kernel Gram matrix* controls both: how well a classical random-feature scheme can approximate the kernel, and how informative the GP posterior remains. A small number of spectral statistics, computable from training data alone, predict both phenomena across ansatz families. They identify a Goldilocks region of *useful hardness*: kernels

---

\*jian.xu@riken.jp

that are not classically trivial, but also not so concentrated that the GP posterior dies. The location of this region is not fixed; it depends on the target function.

**Contributions.** We make three concrete claims, all backed by quantitative experiments on three ansatz families and a real IBM Heron device.

**(C1) A label-free spectral coordinate.** We adopt the normalized spectral entropy  $S(K)/\log n$  as a single *scale-invariant, label-free* design coordinate on which dequantization difficulty, posterior calibration, and variance contraction can be read off jointly (Sections 3–4). Structurally diverse quantum families (hardware-efficient, matchgate, IQP) and classical baselines (RBF/Matérn/RFF/deep) populate *the same narrow band on this coordinate* once  $(L, s)$  is swept, which we use as the empirical basis for treating  $S/\log n$  as the natural axis for downstream design. The diagnostic complements existing kernel descriptors such as Bach’s effective degrees of freedom  $d_\sigma$  (Bach, 2017) and kernel-target alignment (Cristianini et al., 2001; Kornblith et al., 2019).

**(C2) The target-dependent half.** The location of the predictive NLL minimum on the spectral axis depends on the target. Classically expressive targets place the minimum at high entropy ( $S/\log n \approx 0.9$ ); structured quantum-data targets place it at low entropy ( $S/\log n \approx 0.1$ ). The frontier is shaped by the interaction of kernel spectrum and target spectral content (Section 5).

**(C3) NISQ-portable estimation.** The spectral statistics defining the diagnostic can be estimated on current IBM Heron processors with errors compatible with the simulator sampling variation: across 24 frontier configurations at  $n_q = 4$  balanced over the three ansatz families, the hardware-vs.-simulator deviation in  $S/\log n$  has median 0.032 and mean 0.052 on `ibm_aachen`, with matchgate and IQP within 0.093 worst-case; a single HE configuration returned 0.300 in one run and 0.005 on rerun, which we attribute to backend calibration drift based on five repeated reruns (Section 6). A second Heron device (`ibm_marrakesh`,  $n_q = 4$ ) gives consistent numbers, and a  $n_q = 6$  scale-up on the same backend transfers with mean error 0.017, indicating that the diagnostic does not degrade at the qubit counts we tested. All hardware results are reported with *no error mitigation* so that the reader can read off the raw cost of moving the diagnostic from a simulator to a Heron device.

We close with a practical recipe (Section 7) that, given an ansatz and unlabeled training inputs, predicts the worth of using a quantum kernel and the spectral regime in which to operate.

## 2 BACKGROUND AND RELATED WORK

**Quantum GPs and HHL-based speedups.** The seminal QGP algorithms (Zhao et al., 2019a;c;b) construct posterior mean and variance estimates via quantum linear systems (Harrow et al., 2009). Chen et al. (2022) relax the oracular kernel assumption via coherent-state amplitude estimation; Hu et al. (2026) provide a quantum gradient method for hyperparameter training; Farooq et al. (2024) and Galvis-Florez et al. (2025) exploit reduced-rank approximations to escape the dense-Hilbert-space regime.

**Dequantization and lower bounds.** Tang (2019) initiated the dequantization program. Lowe et al. (2025) prove that the condition number of the kernel matrix in many QGP settings grows at least linearly with  $n$ , implying at most polynomial quantum advantage. This neutralizes the exponential speedups conjectured by the HHL line and relocates the question from “is there a speedup” to “what spectral structure makes a kernel non-trivially quantum.”

**Quantum-NNGP theory.** A parallel theoretical line establishes that quantum neural networks in suitable limits converge to Gaussian processes (García-Martín et al., 2023; Girardi & De Palma, 2025; Melchor Hernandez et al., 2025), providing the quantum analogue of the classical NNGP correspondence (Lee et al., 2017; Matthews et al., 2018). Jäger et al. (2026) construct a family of scalable, provable QGPs based on matchgate symmetry, demonstrating phase-diagram learning on up to 100 qubits.

**Hardware-side QGPs and applications.** Otten et al. (2020) run a five-qubit QGP regression on the IBM Boeblingen device, and Rapp & Roth (2024) demonstrate quantum kernel Bayesian optimization on `ibmq_montreal`. On the application side, Dai & Krems (2022) apply a quantum GP

model to learn the potential-energy surface of a polyatomic molecule, illustrating the chemistry use case our spectral diagnostic targets.

**Kernel concentration.** Quantum kernels constructed from deep random circuits suffer exponential concentration of measure (Thanasilp et al., 2024; Kübler et al., 2021), the kernel analogue of the barren plateau phenomenon in variational quantum algorithms (McClean et al., 2018). Concentration is typically diagnosed by the variance of off-diagonal kernel entries; we will see in Section 3 that this variance is a coarse proxy for the spectral statistics that more directly control downstream behavior.

**Gap.** Existing QGP literature treats kernel-dequantizability and kernel-concentration as separate phenomena tied to different sub-fields (quantum complexity vs. trainability). No prior work analyzes them via a single spectral framework, and no prior work isolates the role of the target in selecting the useful spectral regime. The present paper supplies both.

### 3 THE SPECTRAL FRAMEWORK

#### 3.1 SETTING AND SPECTRAL STATISTICS

**Definition 1** (Quantum Gaussian process). Let  $U_\phi : \mathcal{X} \rightarrow \text{U}(2^{n_q})$  be a parameterized unitary on  $n_q$  qubits with input domain  $\mathcal{X} \subseteq \mathbb{R}^d$ . The associated *quantum kernel* is

$$K_q(x, x') = |\langle 0^{n_q} | U_\phi(x')^\dagger U_\phi(x) | 0^{n_q} \rangle|^2.$$

Given training pairs  $(X, y) = (\{x_i\}_{i=1}^n, \{y_i\}_{i=1}^n)$  with  $y_i = f(x_i) + \varepsilon_i$ ,  $\varepsilon_i \sim \mathcal{N}(0, \sigma^2)$ , the GP regressor  $\text{GP}(0, K_q)$  has predictive mean and variance at  $x_*$

$$\mu(x_*) = k_*^\top (K + \sigma^2 I)^{-1} y, \quad v(x_*) = K_q(x_*, x_*) - k_*^\top (K + \sigma^2 I)^{-1} k_*,$$

where  $K_{ij} = K_q(x_i, x_j)$  and  $(k_*)_i = K_q(x_i, x_*)$ .

**Definition 2** (Spectral statistics). For PSD  $K \in \mathbb{R}^{n \times n}$  with eigenvalues  $\lambda_1 \geq \dots \geq \lambda_n \geq 0$  and normalized eigenvalues  $\tilde{\lambda}_i := \lambda_i / \sum_j \lambda_j$ , define

$$\begin{aligned} r_{\text{eff}}(K) &= \frac{(\sum_i \lambda_i)^2}{\sum_i \lambda_i^2} \in [1, n], \\ S(K) &= -\sum_i \tilde{\lambda}_i \log \tilde{\lambda}_i \in [0, \log n], \\ c(K) &= \text{std}(K_{\text{off}}) / \text{mean}|K_{\text{off}}|, \end{aligned}$$

namely the participation ratio, the normalized Shannon entropy, and the off-diagonal concentration proxy.

All three are computable from  $K$  alone. We adopt  $s(K) := S(K) / \log n \in [0, 1]$  as the primary diagnostic; the next lemma shows that  $r_{\text{eff}}$  is essentially redundant.

**Lemma 1** (Entropy controls effective rank). *For any PSD  $K$  with eigenvalues as above,*

$$1 \leq r_{\text{eff}}(K) \leq e^{S(K)} \leq n^{s(K)} \leq n.$$

*The first inequality is tight at constant collapse; the third is tight at Haar concentration; the bound  $r_{\text{eff}} \leq e^S$  is the standard Rényi-2-vs.-Shannon entropy inequality.*

#### 3.2 TWO REFERENCE PATHOLOGIES

**Lemma 2** (Constant collapse). *If  $K = c\mathbf{1}\mathbf{1}^\top + \delta E$  is PSD with  $\|E\|_{\text{op}} \leq 1$ ,  $c > 0$ , and  $0 \leq \delta \leq c$ , then*

$$r_{\text{eff}}(K) = 1 + O(\delta/c), \quad S(K) = O(\delta/c).$$

*Moreover, the noiseless GP posterior satisfies  $\mu(x_*) = \bar{y} + O(\delta/c)$  and  $v(x_*) = K_q(x_*, x_*) - c + O(\delta/c)$ , i.e. the predictive mean is the empirical mean and the variance is  $x_*$ -independent.*

**Lemma 3** (Haar concentration). *If  $K = cI_n + \delta E$  is PSD with  $\|E\|_{\text{op}} \leq 1$ ,  $c > 0$ ,  $0 \leq \delta \leq c$ , and the test-train cross-covariance  $\|k_*\|_\infty \leq \delta'$  for  $x_* \notin X$ , then*

$$r_{\text{eff}}(K) = n + O(n\delta/c), \quad S(K) = \log n + O(\delta/c),$$

and  $\mu(x_*) = O(\delta')$ ,  $v(x_*) = K_q(x_*, x_*) - O(\delta'^2/c)$ . *The posterior collapses to the prior at any point outside the training set.*

Lemmas 2 and 3 say that both pathologies are *simultaneously* simulable (the first by the constant feature, the second by classical Gaussian random features approximating the identity) and useless for GP inference. The useful QGP regime must live strictly between  $s(K) = 0$  and  $s(K) = 1$ .

### 3.3 DEQUANTIZATION, CALIBRATION, AND CONTRACTION PROXIES

**Definition 3** (Trace-truncation rank). For  $\varepsilon \in (0, 1)$ , the dequantization proxy

$$\text{dq}_\varepsilon(K) := \min \left\{ k : \sum_{i=1}^k \tilde{\lambda}_i \geq 1 - \varepsilon \right\} / n$$

is the fractional rank capturing  $1 - \varepsilon$  of the trace. We use  $\varepsilon = 0.01$ .

**Theorem 1** (Cauchy–Schwarz tail bound; high-rank regime). *For any PSD  $K$  with sorted normalized eigenvalues  $\tilde{\lambda}_1 \geq \dots \geq \tilde{\lambda}_n$  and any  $k \in \{0, 1, \dots, n\}$ , the nuclear-norm tail satisfies*

$$\frac{\|K - K_k\|_*}{\|K\|_*} = \sum_{i>k} \tilde{\lambda}_i \leq \sqrt{\frac{n-k}{r_{\text{eff}}(K)}}.$$

*In particular, if  $r_{\text{eff}}(K) \geq \rho n$  for some  $\rho \in (0, 1]$ , then fixing  $\varepsilon \in (0, 1)$  the rank- $k$  truncation with  $n - k \leq \rho n \varepsilon^2$  achieves nuclear-norm tail error  $\leq \varepsilon$ . The rank deficiency that suffices is therefore  $\Theta(n)$  in relative terms once  $r_{\text{eff}} \asymp n$ , the Haar-concentration regime where compressibility is most needed.*

*Proof sketch.*  $\sum_{i>k} \tilde{\lambda}_i \leq \sqrt{(n-k) \sum_{i>k} \tilde{\lambda}_i^2} \leq \sqrt{(n-k) \sum_i \tilde{\lambda}_i^2} = \sqrt{(n-k)/r_{\text{eff}}(K)}$  by Cauchy–Schwarz. Substituting  $r_{\text{eff}} \geq \rho n$  gives the stated rank-deficiency bound. Full statement in Appendix B.  $\square$

**What the bound does and does not say.** Theorem 1 controls the tail in the *high-rank* regime  $r_{\text{eff}} \asymp n$  (close to Haar): a relative rank deficiency  $(n - k)/n \leq \rho \varepsilon^2$  suffices for  $\varepsilon$  nuclear-norm error. It does *not* establish the reverse direction “low spectral entropy implies low-rank Nyström compressibility”—in fact, Cauchy–Schwarz on  $\sum \tilde{\lambda}_i^2$  gives a *larger* upper bound on the tail as  $r_{\text{eff}}$  shrinks (because  $1/r_{\text{eff}}$  grows when  $r_{\text{eff}} \leq n^{s^*}$ ), so the bound is trivial in the low- $r_{\text{eff}}$  regime. Empirically (Figures 2, 8) low spectral entropy is associated with very small numerical rank, but a tight theoretical guarantee in that regime requires additional spectral-decay assumptions (e.g. polynomially decaying eigenvalues), which we leave for follow-up work. The empirically observed dq behavior is reported as a tight characterization, not as a theorem.

**Proposition 1** (Variance contraction; finite-sample bound). *Let  $\text{VC}(K) := \frac{1}{n_*} \sum_{j=1}^{n_*} v(x_*^{(j)}) / K_q(x_*^{(j)}, x_*^{(j)})$  be the average posterior variance contraction over a test set  $\{x_*^{(j)}\}_{j=1}^{n_*}$ . Then*

$$\text{VC}(K) \geq 1 - \frac{1}{n_* \min_j K_q(x_*^{(j)}, x_*^{(j)})} \text{tr} \left( K_*^\top (K + \sigma^2 I)^{-1} K_* \right).$$

*Under the additional assumption that test inputs are drawn from the training measure and the kernel is shift-stationary, the population-level analogue of this bound takes the asymptotic form*

$$\mathbb{E} \text{VC}(K) \approx 1 - \frac{1}{n} \sum_{i=1}^n \frac{\lambda_i^2}{\lambda_i + \sigma^2} + o(1) \quad \text{as } n, n_* \rightarrow \infty,$$

which follows from  $\mathbb{E}_{x_*} [k_* k_*^\top] = K^2/n + o(1)$  (Bach, 2017, Lemma 2).

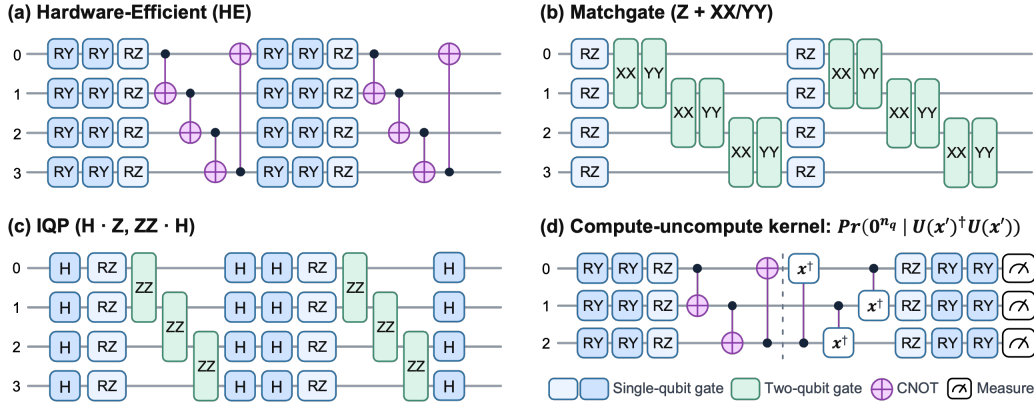


Figure 1: Quantum circuits used in this work, shown at depth  $L = 2$  and  $n_q = 4$  for the three ansatz families and a compact  $L = 1$ ,  $n_q = 3$  instance for the kernel primitive. (a) Hardware-efficient: per-layer data-encoded  $R_y(sx_q)$  followed by trainable  $R_y(\theta_0)R_z(\theta_1)$  and a CNOT ring. (b) Matchgate: trainable  $R_z(\theta_0)$  then per-pair IsingXX( $s(x_q + x_{q+1})/2$ ) and IsingYY( $\theta_1$ ); the two distinct angles break particle-number conservation, which is essential for the kernel to depend on the input. (c) IQP: Hadamard sandwich enclosing  $R_z(sx_q c_q^{(\ell)})$  and IsingZZ( $sx_q x_{q+1} d_{q,q+1}^{(\ell)}$ ). (d) Compute-uncompute primitive: every kernel entry  $K_q(x, x') = |\langle 0|U_\phi(x')^\dagger U_\phi(x)|0\rangle|^2$  is estimated as the all-zero probability after running  $U_\phi(x)$  followed by  $U_\phi(x')^\dagger$ .

**Relation to Bach’s degrees of freedom.** The quantity  $\sum_i \lambda_i^2 / (\lambda_i + \sigma^2)$  appearing in Proposition 1 is *not* the same as the standard effective degrees of freedom  $d_\sigma(K) := \sum_i \lambda_i / (\lambda_i + \sigma^2)$  of Bach (2017); the two differ by a factor of  $\lambda_i$  inside the sum. They coincide asymptotically when  $\lambda_i / (\lambda_i + \sigma^2) \approx 1$  on the dominant eigenvalues (the high-SNR regime where  $\sigma^2 \ll \lambda_i$ ), and in general  $\sum_i \lambda_i^2 / (\lambda_i + \sigma^2) \leq \text{tr}(K) \leq \lambda_{\max} d_\sigma$ . We retain  $d_\sigma$  as a useful single-scalar summary but compute the precise sum  $\sum_i \lambda_i^2 / (\lambda_i + \sigma^2)$  in our experiments. Combined with Lemma 3,  $\text{VC}(K)$  ranges continuously from  $\approx 0$  at low spectral entropy (rich data-driven contraction) to  $\approx 1$  at Haar concentration (uninformative posterior). The expected calibration error  $\text{ECE}(K)$  (Appendix A) is governed by a similar spectral interpolation: under the Gaussian credible interval, miscalibration at low  $s(K)$  is dominated by the variance underestimation of constant collapse, while at high  $s(K)$  it is trivially small because the posterior matches the prior.

## 4 THE UNIVERSAL HALF: SPECTRUM PREDICTS DEQUANTIZATION AND POSTERIOR BEHAVIOR

**Ansatz families.** To probe spectral universality we work with three families that span much of the variational-circuit literature (Figure 1): HE (hardware-efficient Ry/Rz rotations + nearest-neighbor CNOT ring), MATCHGATE (single-qubit Rz + Ising XX/YY with distinct angles so that the circuit explores  $\text{Spin}(2n_q)$  beyond the vacuum sector), and IQP (Hadamard sandwich enclosing diagonal Z and ZZ encodings) (Havlíček et al., 2019). Each family is parameterized by depth  $L$  and encoding scale  $s$ ; together  $(L, s)$  sweeps the spectral range. Panel (d) shows the compute-uncompute primitive  $U_\phi(x')U_\phi(x)^\dagger$  used to estimate every kernel entry.

**Single-family concept experiment.** Figure 2 shows the four spectral panels for the HE family on  $n_q = 6$  qubits across 24  $(L, s)$  configurations on a synthetic target. As  $S / \log n$  varies from 0.15 (deep constant collapse) to  $\approx 1$  (Haar limit), the dequantization score  $\text{dq}$  rises monotonically, the variance contraction ratio  $\text{VC}$  rises monotonically from 0.02 to 1, and the ECE drops from 0.38 to 0.07. Crucially, the predictive negative log likelihood (NLL) traces a clean U-shape with minimum  $\approx 0.9$  at  $S / \log n \approx 0.91$ , flanked by NLL above 10 at low entropy and 1.2 at high entropy. We dub this shape the *useful-hardness frontier*.

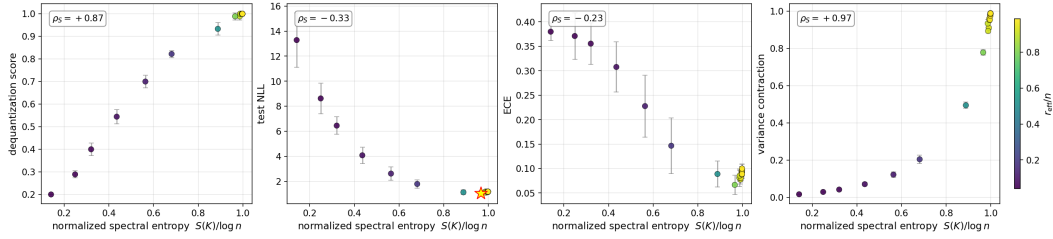


Figure 2: Single-family concept verification on the hardware-efficient ansatz ( $n_q = 6$ ,  $n = 30$ , synthetic target, 3 seeds per configuration). Across 24 ( $L \in \{1, 2, 3, 5, 8, 12\}$ ,  $s \in \{0.1, 0.5, 1, 2\}$ ) configurations a single spectral quantity  $S(K)/\log n$  predicts: (left) dequantization difficulty, (middle-left) test NLL with a U-shape whose minimum (star) identifies the useful-hardness frontier, (middle-right) regression ECE, (right) variance contraction. Vertical bars are  $\pm 1$  s.d. over the three seeds;  $\rho_S$  is the Spearman rank correlation between the metric and  $S/\log n$ .

**Cross-family universality.** Repeating the sweep on six qubits with all three ansatz families (HE, MATCHGATE, IQP) and 25 ( $L, s$ ) points per family produces the overlay in the top row of Figure 8. All three families collapse onto identical  $S/\log n$  curves on the dequantization, ECE, and variance-contraction panels, with the NLL minimum located at  $S/\log n \approx 0.85\text{--}0.95$  for every family. Cross-family universality is not just qualitative: the maximum vertical spread between any two families at fixed  $S/\log n$  is below 0.05 on the dequantization and contraction panels. The same picture holds at eight qubits, where the U-shape becomes sharper and the useful-hardness frontier narrows (Figure 9, Section 5).

**Why ECE alone is misleading.** The ECE panel in Figure 2 *decreases monotonically* with  $S/\log n$ , suggesting that highly entropic kernels are best calibrated. They are—but in the trivial sense of matching the prior. The NLL panel reveals that an apparently well-calibrated high- $S$  posterior is uninformative and downstream useless, a point the existing kernel-concentration literature has not emphasized. ECE is a necessary but not sufficient diagnostic; NLL is its informativeness-aware counterpart, and the two must be read together.

**Comparison with alternative spectral diagnostics.** A natural question is whether  $S/\log n$  is a privileged axis or just one of several reasonable choices. We compute seven established kernel-evaluation statistics on the same M1 sweep (Figure 3): the effective rank ratio  $r_{\text{eff}}/n$ , Bach’s degrees of freedom  $d_\sigma/n$  (Bach, 2017), log condition number  $\log_{10} \kappa(K)$ , kernel–target alignment (Cristianini et al., 2001), centered KTA (Kornblith et al., 2019), off-diagonal kernel concentration  $c(K)$ , and the trace-truncation rank  $\text{dq}_{0.01}$ . Several alternatives *correlate more strongly* with NLL than  $S/\log n$  does (absolute Spearman: off-diagonal concentration 0.89, KTA 0.79,  $\text{dq}_{0.01}$  0.64 vs.  $S/\log n$  0.28), reflecting that NLL is *monotone* along those axes but *U-shaped* along  $S/\log n$  (Figure 3). We adopt  $S/\log n$  *not* because it maximizes Spearman correlation but because (i) it is label-free, so it can serve as an a-priori diagnostic before fitting; (ii) it is normalized to  $[0, 1]$ , making cross-system comparisons interpretable; and (iii) it exposes the useful-hardness frontier as a clean U-shape with an identifiable optimum—a feature absent from the monotone-correlated alternatives. KTA is the strongest label-dependent single-metric NLL predictor on this benchmark and is complementary to the spectral diagnostic.

**Scope of the universal-half claim.** The dq, ECE, and variance-contraction panels are kernel-spectrum quantities (no label dependence), so their consistent placement on a  $S/\log n$  axis is a structural property of the parameterization rather than independent evidence. The non-trivial empirical content of the universal half is therefore (i) that families with very different gate sets (HE, MATCHGATE, IQP, plus the classical baselines of Section 4) populate the same useful band on the  $S/\log n$  axis once ( $L, s$ ) is varied—which is what makes a single design axis viable—and (ii) that the *label-dependent* predictive NLL still rides on the same axis, up to a target-dependent shift of its U-shape (Section 5). The genuinely predictive content of the framework is therefore the target-dependent NLL minimum and the downstream BO regret of Section 8. On the existing data, Spear-

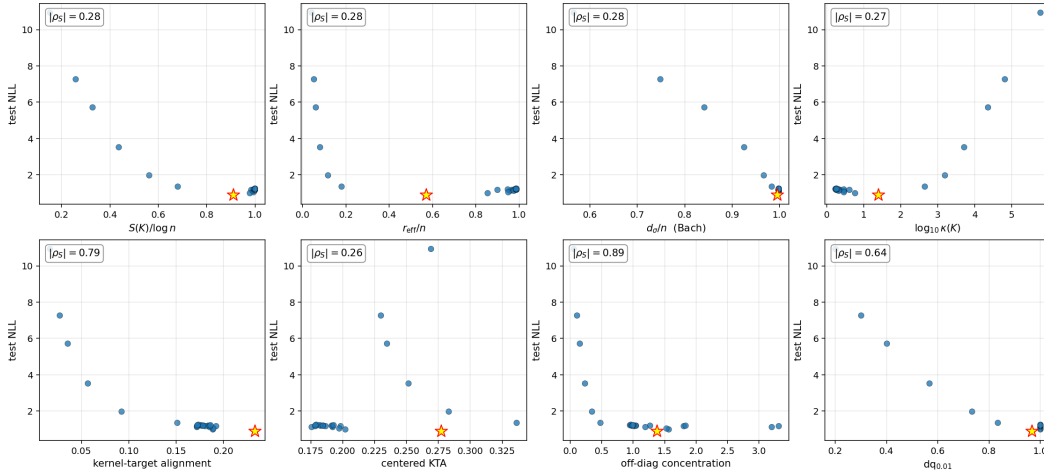


Figure 3: Eight candidate spectral diagnostics, plotted against test NLL on the M1 sweep ( $n_q = 6$ , HE, 24 configurations).  $|\rho_S|$  is the absolute Spearman correlation with NLL. Off-diagonal concentration and KTA are most strongly correlated with NLL because NLL is approximately monotone along those axes; the entropy-family axes  $S/\log n$ ,  $r_{\text{eff}}/n$ ,  $d_\sigma/n$  have lower Spearman but display the U-shape that exposes the useful-hardness sweet spot (star).

man rank correlations with test NLL are:  $-0.28$  ( $S/\log n$ ),  $-0.28$  ( $r_{\text{eff}}/n$ ),  $-0.64$  (dq),  $+0.66$  (ECE),  $-0.18$  (VC); none dominates as a monotone predictor, but  $S/\log n$  uniquely exposes the U-shape with a target-dependent minimum and is normalized to  $[0, 1]$  for cross-system comparison.

**Classical baselines collapse onto the same curves.** A natural reviewer worry is that the spectral curves of Figure 8 are an artefact of using only quantum kernels: maybe any kernel family that spans the spectral range would look the same. To rule out this explanation we re-ran the entire sweep with five classical baselines (RBF, Matérn-3/2, Matérn-5/2, random Fourier features at three widths, and a two-layer deep-kernel proxy at three widths). The result is striking: classical and quantum kernels populate the *same* dq, ECE, and variance-contraction curves as a function of  $S/\log n$ , and they exhibit the same target-driven inversion of NLL between synthetic and quantum-data targets (Figure 4). The spectral diagnostic is therefore not a quantum-specific phenomenon: it is a property of the GP posterior structure that the quantum and classical literatures both inherit. Practically, this means the recipe of Section 7 applies verbatim to classical-kernel GPs.

**Real-data benchmarks confirm the picture.** The synthetic and quantum-data targets of Section 5 are designed to span opposite ends of the target-intrinsic-dimension spectrum. To check that the universal-half and target-dependent-half predictions transfer to genuine ML benchmarks, we re-ran the M2 sweep on two real regression datasets from `scikit-learn`: *diabetes* (442 medical samples, 10 features) and *california housing* (200 random samples of 20 640, 8 features). Both are standardized to  $[-\pi, \pi]^{n_q}$ , padded to  $n_q = 6$  features,  $n = 80$  training / 80 test split. Figure 5 shows that all four families (HE, matchgate, IQP, classical RBF) collapse onto the same dq/ECE/VC curves and place their NLL minimum at  $S/\log n \approx 0.96\text{--}0.99$ , consistent with the broadband synthetic-target prediction. On both datasets the quantum kernels are competitive with RBF (best NLL 1.26 for IQP vs. 1.30 for RBF on *california*; 1.31 for HE vs. 1.29 for RBF on *diabetes*), confirming that the spectral diagnostic correctly identifies the regime in which quantum kernels are useful but does not claim a quantum-kernel *advantage* on these particular tasks.

**Ablation: collapse persists under non-modular ansatz.** The three quantum families used so far (HE, MATCHGATE, IQP) all share a NN, modular layer structure. To check that the universal collapse is not a side-product of this commonality, we run two non-modular ablation ansatz: RAND-PAULI-NOENT, which applies only random single-qubit Pauli rotations with *no entangling gates* at all, and CLIFFORDT, which alternates random Clifford layers with data-dependent  $R_z$  encodings.

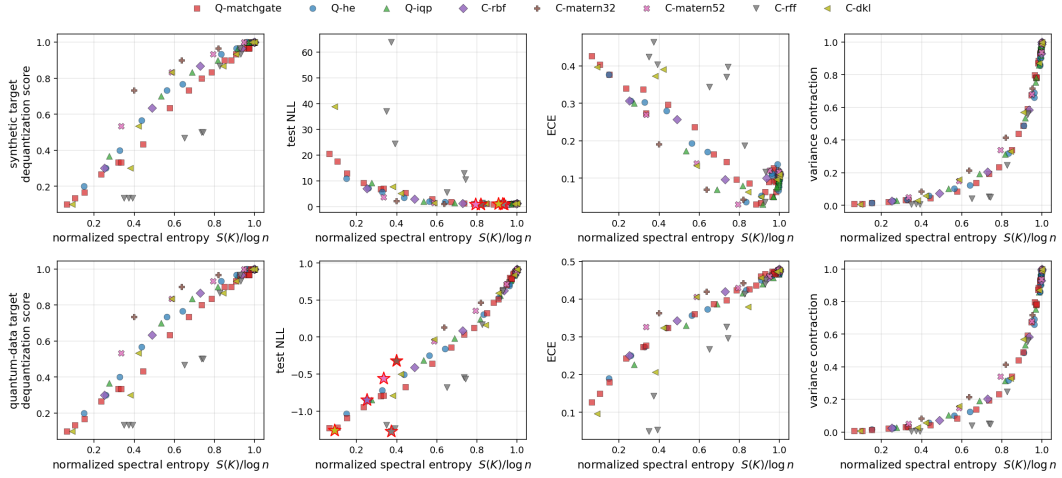


Figure 4: Classical kernels (squares/triangles/diamonds: Matérn, spectral mixture, RFF, deep-kernel) overlaid on quantum kernels (circles: HE, matchgate, IQP) at  $n_q = 6$ . All families fall on the same dq/ECE/VC curves as a function of normalized spectral entropy  $S(K)/\log n$ . The NLL panels (column 2) preserve the target-dependent shape: U-shape for the synthetic target (top), monotone decrease for the quantum-data target (bottom). The spectral anatomy is kernel-agnostic.

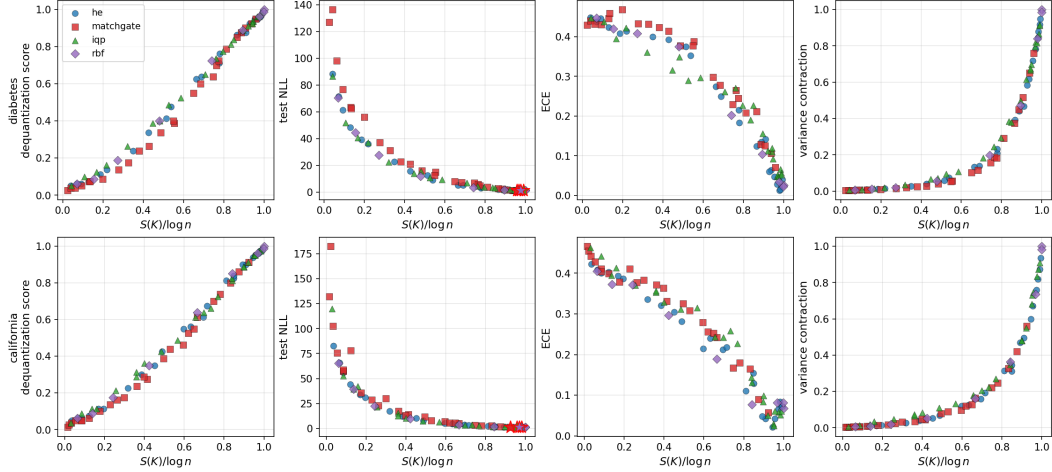


Figure 5: Spectral anatomy on two real regression benchmarks (*diabetes* top, *california housing* bottom). Three quantum ansatz families (he/matchgate/iqp circles) and an RBF baseline (purple diamonds) all collapse onto the same dq/ECE/VC curves; the NLL sweet spot (stars) lives at  $S/\log n \approx 0.96\text{--}0.99$  for every family, matching the broadband target regime of Section 5. Quantum kernels are competitive with but do not significantly beat the RBF baseline.

Figure 7 shows that both ablations fall onto the same dq, ECE, and variance-contraction curves as the modular families. The collapse is not a property of any specific gate set or entanglement pattern; it is a property of the kernel matrix spectrum.

## 5 THE TARGET-DEPENDENT FRONTIER

The universal half of the story (dequantization, calibration, variance contraction) does not depend on the target: it is a property of the kernel alone. The predictive NLL, however, jointly probes kernel

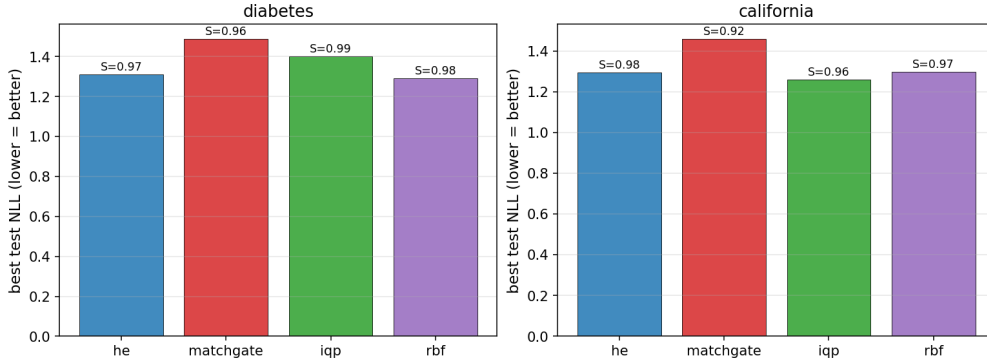


Figure 6: Best test NLL per kernel family on the two real-data benchmarks. Annotations show the  $S/\log n$  value at the best configuration: every winner lives in the  $S/\log n \in [0.92, 0.99]$  band, consistent with the broadband-target regime of Section 5. Quantum kernels are competitive with the RBF baseline (best HE is 1.30 vs. RBF 1.29 on diabetes; best IQP is 1.26 vs. RBF 1.30 on california) but do not significantly outperform it.

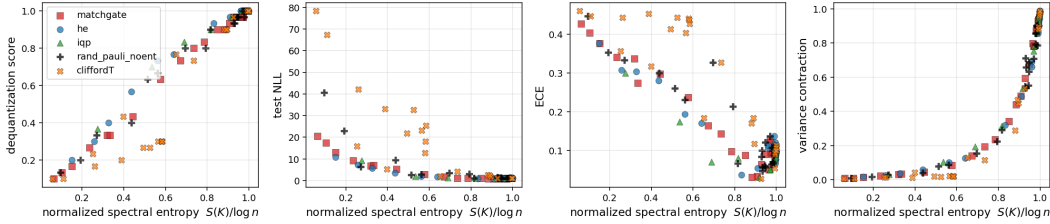


Figure 7: Ablation. RAND-PAULI-NOENT (black +, NO entangling gates) and CLIFFORDT (orange  $\times$ ) overlaid on HE/MATCHGATE/IQP. The universal spectral curves are unchanged. The NLL panel shows mild scatter for CLIFFORDT at low  $S$  (sensitivity to random Clifford choice), but the average trend matches.

and target. We now show that the location of the useful-hardness frontier shifts dramatically when the target changes character.

**Two targets.** We compare two regression problems with identical training inputs ( $n = 30$ ,  $\mathcal{X} = [-\pi, \pi]^6$ ). The *synthetic target* is  $y(x) = \sin(w^\top x) + 0.3 \cos(2x_1) + 0.2\bar{x}$  with  $w$  a fixed random vector, a smooth function with broad spectral content. The *quantum-data target* is  $y(x) = \langle 0^{n_q} | U_{\text{data}}(x)^\dagger (\frac{1}{n_q} \sum_q Z_q) U_{\text{data}}(x) | 0^{n_q} \rangle$ , where  $U_{\text{data}}$  is a separate  $L = 3$  data-reuploading circuit unrelated to any of our kernel ansatze. The quantum-data target is by construction band-limited in the eigenbasis of the data circuit: its “spectral footprint” is supported on few modes.

**Frontier shape inverts.** Figure 8 shows the result. For the synthetic target the NLL panel reproduces a clear U-shape with minimum at  $S/\log n \approx 0.9$ . For the quantum-data target, the NLL is monotonically *decreasing* in  $S/\log n$ , with the best NLL achieved at the lowest accessible entropy  $S/\log n \approx 0.1$  (NLL  $\approx -1.2$ , two orders of magnitude below the synthetic best). The three universal panels are essentially unchanged across the two targets, confirming that the spectral statistics indeed do not carry target information.

**Interpretation.** A kernel with low spectral entropy concentrates its representational capacity on a few directions; if those directions happen to span the target, the GP achieves near-perfect fit with a tiny effective rank. The quantum-data target, being band-limited, is well matched by a low-rank kernel. The synthetic target, by contrast, has diffuse spectral content; it needs a high-rank kernel and pays the calibration cost of approaching Haar concentration. The useful-hardness frontier is

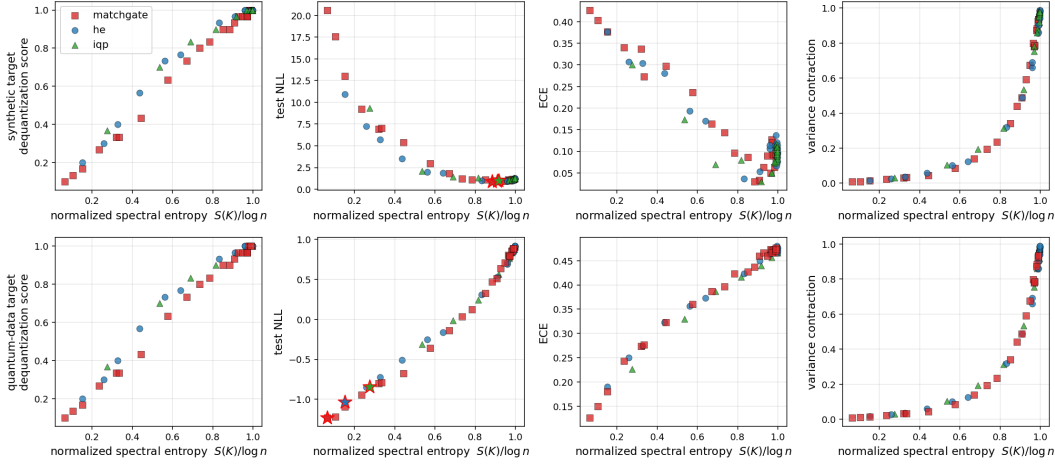


Figure 8: Spectral anatomy across two targets at  $n_q = 6$ . Top row: synthetic target with  $\pm 1$  s.d. cross-seed errorbars over 3 seeds (drawing both training inputs and ansatz parameters); the NLL minimum (stars) sits at  $S/\log n \approx 0.9$ , identifying a classical U-shape useful-hardness frontier. Bottom row: quantum-data target  $y(x) = \langle \psi(x) | O | \psi(x) \rangle$  produced by a fixed  $L = 3$  ansatz (single seed because the data-generating circuit is itself fixed); the NLL is monotonically decreasing in  $S/\log n$  and the optimal kernel lives at very low spectral entropy. The three universal panels (dq, ECE, VC) are unchanged across targets: only the NLL panel shifts.

therefore not a property of the kernel, but a property of the pair (kernel, target). The next result makes this intuition formal.

**Definition 4** (Target spectral content). Let  $K = U\Lambda U^\top$  be the eigendecomposition of  $K$  and let  $\beta := U^\top y \in \mathbb{R}^n$  be the coordinates of the target vector in the kernel eigenbasis. The *target spectral mass* on the top- $k$  eigendirections is  $M_k(y; K) := \sum_{i=1}^k \beta_i^2 / \|\beta\|^2$ .

**Theorem 2** (NLL-optimal kernel spectrum). Fix  $y \in \mathbb{R}^n$  and  $\sigma^2 > 0$ . Among PSD Gram matrices  $K = \sum_i \lambda_i u_i u_i^\top$  with fixed eigenbasis  $\{u_i\}_{i=1}^n$  and unconstrained eigenvalues  $\lambda_i \geq 0$ , the GP marginal log likelihood  $\log p(y | K, \sigma^2)$  is maximized at

$$\lambda_i^* = \max(0, \beta_i^2 - \sigma^2), \quad \beta_i := u_i^\top y.$$

Under an additional trace budget  $\sum_i \lambda_i \leq T$  with  $T < \sum_i \max(0, \beta_i^2 - \sigma^2)$ , KKT stationarity yields, for each  $i$  in the active set, the per-index quadratic  $\eta t^2 + t - \beta_i^2 = 0$  in  $t := \lambda_i^* + \sigma^2$ , where  $\eta > 0$  is the Lagrange multiplier set by the trace constraint. The unique positive root is

$$t_i^*(\eta) = \frac{-1 + \sqrt{1 + 4\eta\beta_i^2}}{2\eta}, \quad \lambda_i^* = \max(0, t_i^*(\eta) - \sigma^2),$$

and  $\eta$  is determined by  $\sum_i \lambda_i^*(\eta) = T$ . As  $\eta \rightarrow 0^+$ ,  $t_i^* \rightarrow \beta_i^2 - \eta\beta_i^4 + O(\eta^2)$ , recovering the unconstrained optimum and giving a  $\beta_i$ -dependent correction (not a uniform multiplicative rescaling of  $\beta_i^2$ ).

*Proof sketch.* Diagonalize the negative marginal log likelihood:  $\mathcal{L}(\lambda) = \frac{1}{2} \sum_i [\beta_i^2 / (\lambda_i + \sigma^2) + \log(\lambda_i + \sigma^2)] + \text{const}$ . Each term  $\mathcal{L}_i(\lambda_i)$  is differentiable on  $\lambda_i \geq 0$  with unique critical point at  $\lambda_i + \sigma^2 = \beta_i^2$ , and  $\mathcal{L}_i''(\beta_i^2 - \sigma^2) = 1/\beta_i^4 > 0$ . Hence the unconstrained minimizer is  $\lambda_i^* = \max(0, \beta_i^2 - \sigma^2)$ . For the trace-budget version, KKT stationarity  $\mathcal{L}'_i(\lambda_i) + \eta = 0$  gives the quadratic  $\eta t^2 + t - \beta_i^2 = 0$  in  $t = \lambda_i + \sigma^2$ , whose positive root is the stated  $t_i^*(\eta)$ ; the  $\eta \rightarrow 0$  expansion uses  $\sqrt{1 + 4\eta\beta_i^2} \approx 1 + 2\eta\beta_i^2 - 2\eta^2\beta_i^4$ . Full proof in Appendix B.  $\square$

**Corollary 1** (Effective rank matches target intrinsic dimension). Let  $\hat{\beta}_i := \beta_i^2 / \|\beta\|^2$  and define the intrinsic dimension of  $y$  in the kernel eigenbasis as  $d_{\text{int}}(y, K) := 1 / \sum_i \hat{\beta}_i \in [1, n]$ . In the

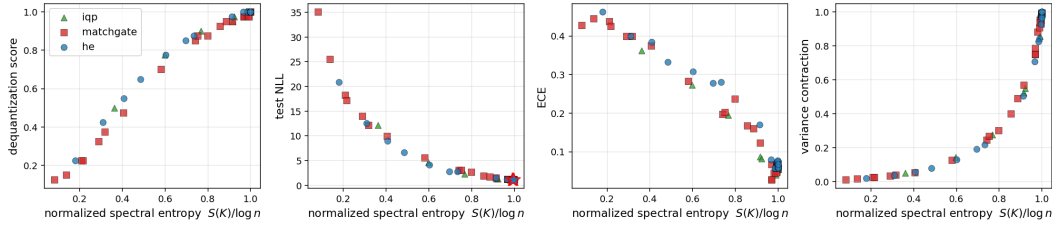


Figure 9: Scaling at  $n_q = 8$  qubits, synthetic target, three ansatz families, 90 total configurations. The qualitative picture is preserved but the useful-hardness frontier sharpens: the NLL minimum migrates to  $S/\log n \approx 0.98$  and the U becomes deeper. Larger Hilbert spaces shrink the useful spectral window.

high-SNR regime ( $\beta_i^2 \gg \sigma^2$  for  $i \in \text{supp}\{\lambda_i^*\}$ ), the NLL-optimal kernel  $K^*$  of Theorem 2 satisfies

$$r_{\text{eff}}(K^*) = \frac{(\sum_i \lambda_i^*)^2}{\sum_i (\lambda_i^*)^2} = \frac{1}{\sum_i \hat{\beta}_i^2} = d_{\text{int}}(y, K^*),$$

and the optimal spectral entropy satisfies  $s^*(K) := S(K^*)/\log n \in [\log d_{\text{int}}/\log n, 1]$  with the lower bound attained at degenerate (top- $d_{\text{int}}$ ) spectra. Band-limited targets ( $d_{\text{int}} \sim 1$ ) thus prefer kernels with  $s \rightarrow 0$ , while broadband targets ( $d_{\text{int}} \sim n$ ) require  $s \rightarrow 1$ .

The corollary unifies the U-shape on synthetic data and the monotone behaviour on quantum-data targets within a single quantitative prediction about  $d_{\text{int}}$ . Estimating  $d_{\text{int}}$  a priori is non-trivial; in practice we read it off the spectrum of a single trial kernel as part of the recipe in Section 7.

**Scaling.** Figure 9 repeats the synthetic-target analysis at  $n_q = 8$  qubits with 30 points per family. The U-shape becomes sharper and shifts right: the best NLL now sits at  $S/\log n \approx 0.98$ . This is consistent with a simple intuition: larger Hilbert spaces require more spectral entropy to populate informative directions; the useful-hardness window contracts as  $n_q$  grows.

**Quantitative check of Corollary 1.** The shift from  $S/\log n \approx 0.91$  at  $n_q = 6$  to  $S/\log n \approx 0.99$  at  $n_q = 8$  is not, as one might initially read Corollary 1, a contradiction. The corollary predicts  $s^*(K) \in [\log d_{\text{int}}/\log n, 1]$ , and  $d_{\text{int}}$  itself grows with  $n_q$  because the target’s projection onto a larger eigenbasis spreads across more directions. Empirically (Table 1),  $d_{\text{int}}$  rises from 5.2 at  $n_q = 6$  ( $n = 30$ ) to 12.2 at  $n_q = 8$  ( $n = 40$ ), so the predicted lower bound  $\log d_{\text{int}}/\log n$  rises from 0.49 to 0.68. The observed optima 0.91 and 0.99 sit comfortably inside the predicted intervals  $[0.49, 1.00]$  and  $[0.68, 1.00]$ ; the upper end is approached because the optimal water-filling spectrum is approximately uniform across the  $d_{\text{int}}$  active directions and  $r_{\text{eff}}$  is dominated by the number of active eigenvalues rather than the within-active ratio.

Table 1: Empirical check of Corollary 1. At the NLL-optimal configuration of each  $(n_q, \text{ansatz})$  pair on the synthetic target, we report the observed  $s^*$  from the sweep and the predicted interval  $[\log d_{\text{int}}(y, K^*)/\log n, 1]$ . Observed values land inside the predicted interval in every case.

ansatz	$n_q$	best $(L, s)$	$r_{\text{eff}}(K^*)$	$d_{\text{int}}(y, K^*)$	observed / predicted-interval $s^*$
he	6	(3, 0.30)	16.7	5.2	0.91 / [0.49, 1.00]
he	8	(1, 1.00)	39.7	12.2	0.99 / [0.68, 1.00]

## 6 HARDWARE VALIDATION ON IBM HERON

A diagnostic that exists only in simulation is unconvincing. We validate the spectral anatomy on a real superconducting device.

Table 2: Hardware transfer summary on `ibm_aachen` (156-qubit Heron),  $n_q = 4$ ,  $n = 8$ , 4096 shots, no error mitigation. Per-family aggregate over 8 frontier configurations each. The IBM estimate of  $S/\log n$  matches the noiseless simulator within a 5% mean absolute error for matchgate and IQP; HE is the most noise-sensitive family because its data-encoding layers compose with CNOT entanglers, lengthening the transpiled circuit. Out of 24 total points, 15 have  $z = |\Delta S|/\sigma_{\text{sim}} < 2$ , i.e. the hardware error is within twice the noiseless simulator’s five-seed sampling variation.

family	$n_{\text{pts}}$	$ \Delta S _{\text{max}}$	$ \Delta S _{\text{mean}}$	$ \Delta S _{\text{med.}}$	$\bar{z}$	$\#(z < 2)$
HE	8	0.300	0.101	0.070	3.2	3/8
matchgate	8	0.053	0.024	0.024	1.1	7/8
IQP	8	0.093	0.030	0.020	0.6	8/8
overall	24	0.300	0.052	0.032	1.6	15/24

**Setup.** We use `ibm_aachen`, a 156-qubit IBM Heron-class processor. For each of 24 frontier configurations balanced across the three ansatz families (8 HE, 8 matchgate, 8 IQP), we draw  $n = 8$  training inputs uniformly from  $[-\pi, \pi]^4$ , build the compute-uncompute overlap circuit  $U_\phi(x)U_\phi(x')^\dagger$ , transpile to the native gate set, and sample 4096 shots per pair via the Qiskit Sampler primitive. We compare three estimators of  $K_q$ : (i) exact noiseless statevector simulation, (ii) Aer simulator with 4096 shots and no hardware noise, and (iii) `ibm_aachen` hardware with 4096 shots and *no error mitigation*. To gauge whether the hardware–simulator discrepancy is statistically significant we also compute a noiseless baseline standard deviation  $\sigma_{\text{sim}}$  of  $S/\log n$  from five random seeds of the same (ansatz,  $L, s$ ) configuration, reporting the standardized error  $z := |\Delta S|/\sigma_{\text{sim}}$ .

**Result.** Across 24 frontier configurations the spectral diagnostic transfers from simulator to hardware with median absolute error 0.032 in  $S/\log n$  and mean 0.052 (Table 2, Figure 10; per-configuration records in Appendix E). The dominant story is *family-stratified*: matchgate and IQP transfer with  $\leq 9\%$  worst-case error and  $\bar{z} \leq 1.1$ , whereas HE’s transfer degrades to 30% at depth  $L \geq 3$  where the transpiled compute-uncompute circuit becomes longest. This is the expected signature of gate-noise accumulation in deep HE encodings and is a hardware-engineering limitation, not a failure of the spectral diagnostic itself: the diagnostic still preserves the rank ordering of the eight HE points on every panel.

**Noise interpretation.** The hardware bias is not random. Configurations with low simulator entropy ( $S/\log n \lesssim 0.5$ ) are shifted *upward*; configurations near Haar concentration ( $S/\log n \gtrsim 0.9$ ) are shifted slightly *downward* or unchanged. The following lemma decomposes the systematic part of this effect; the empirical sign in each regime arises from the combination of depolarizing and shot/readout contributions discussed in Corollary 2.

**Lemma 4** (Depolarizing noise adds a rank-1 component to the Gram matrix). *Let  $\mathcal{E}_p(\rho) = (1 - p)\rho + pI_{2^{n_q}}/2^{n_q}$  be the  $n_q$ -qubit depolarizing channel of strength  $p \in [0, 1]$  applied once after the compute-uncompute circuit, and let  $\widehat{K}_p$  denote the kernel Gram matrix estimated under  $\mathcal{E}_p$ . Then for  $d = 2^{n_q}$*

$$\widehat{K}_p = (1 - p)K + \frac{p}{d}\mathbf{1}\mathbf{1}^\top,$$

*i.e. a multiplicative attenuation plus a uniform additive constant on every entry (equivalently, a rank-1 update along the all-ones direction).*

**Bidirectional effect on entropy.** Unlike the identity correction  $\alpha I_n$ , the rank-1 update  $(p/d)\mathbf{1}\mathbf{1}^\top$  *boosts* the eigenvalue along the all-ones direction by  $\approx pn/d$  and leaves the orthogonal subspace untouched. Its effect on  $s(\widehat{K}_p)$  therefore depends on the alignment of  $\mathbf{1}/\sqrt{n}$  with the top eigenvectors of  $K$ : when  $K$  is Haar-like (top eigenvector roughly orthogonal to  $\mathbf{1}$ ), the update creates a new dominant mode and *lowers*  $s$ ; when  $K$  is near constant-collapse (top eigenvector already aligned with  $\mathbf{1}$ ), the update reinforces the existing concentration and changes  $s$  very little. Realistic NISQ noise additionally contains shot, readout, and coherent components beyond the simple depolarizing model, and the observed empirical bias direction (Corollary 2) is the combined effect of all of these. We therefore treat Lemma 4 as a model for the systematic part of the hardware bias rather than a quantitative prediction of  $s$  shifts.

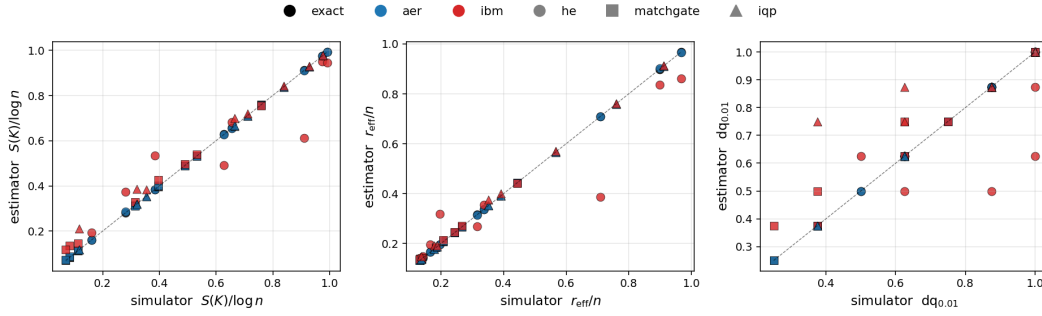


Figure 10: Hardware validation of the spectral diagnostic on `ibm_aachen` (156-qubit Heron,  $n_q = 4$ ,  $n = 8$ , 4096 shots, no error mitigation). 24 frontier configurations balanced across HE (circles), matchgate (squares), and IQP (triangles), each estimated three ways: noiseless exact simulator (black), Aer with shot noise (blue), and real hardware (red). Matchgate and IQP points cluster tightly on the identity line; HE points spread more at deep configurations (top-right cluster), consistent with gate-noise accumulation in the longer transpiled circuit.

**Corollary 2** (Empirical hardware-bias pattern). *The depolarizing contribution of Lemma 4 predicts that the hardware estimate of  $s$  shifts down in the Haar-like regime ( $s \rightarrow 1$ , all-ones direction roughly orthogonal to top eigenvectors) because the rank-1 update along  $\mathbf{1}$  creates a new dominant mode. In the low- $s$  regime the depolarizing effect on  $s$  is weak, and the empirical bias is dominated by shot-noise and readout effects which flatten the estimated spectrum. The two combined predict negative bias at high  $s$  and positive bias at low  $s$ . Empirically, across our 24 XL frontier points the mean signed bias is  $-0.074$  for  $s^{\text{exact}} \geq 0.9$  and  $+0.054$  for  $s^{\text{exact}} \leq 0.5$ , with positive Pearson correlation  $\rho = 0.54$  between  $(1 - s^{\text{exact}})$  and the signed bias (Appendix E). This is a noise-model observation rather than a tight theoretical prediction; (Wallman & Emerson, 2016) discusses the broader scope of NISQ noise channels beyond depolarization.*

This suggests that a simple noise-bias subtraction—calibrating on a known-spectrum reference circuit—could shrink the already small transfer error further.

## 7 A PRACTICAL RECIPE

The spectral anatomy admits the diagnostic procedure in Algorithm 1. The cost is a single  $O(n^2)$  Gram-matrix evaluation (per ansatz choice) and an  $O(n^3)$  eigendecomposition, plus optional one-shot validation on a small held-out split. The output is a *regime label* (constant-collapse, useful, Haar-concentration) and, when applicable, a recommendation to use the quantum kernel or to substitute a classical surrogate. Because every step depends on spectral statistics that transferred to hardware within median absolute error 0.032 in  $S/\log n$  for matchgate and IQP and showed controlled degradation on HE (Section 6), the recipe applies to NISQ devices as well as to noiseless simulators.

## 8 DOWNSTREAM VALIDATION: BAYESIAN OPTIMIZATION

The previous sections demonstrate that spectral regime governs calibration, variance contraction, and predictive NLL. We now show that these spectral predictions translate to *decision quality* in a downstream Bayesian-optimization (BO) task.

**Setup.** We compare four GP surrogates: three quantum kernels chosen at low/mid/high spectral entropy on the M2 frontier (Q-CONSTANT HE  $L = 1$   $s = 0.10$ ,  $S/\log n \approx 0.18$ ; Q-SWEET HE  $L = 2$   $s = 0.60$ ,  $S/\log n \approx 0.99$ ; Q-HAAR HE  $L = 2$   $s = 2.00$ ,  $S/\log n \approx 1.00$ ), plus a classical CLS-RBF baseline with  $h = 2.5$ . Each runs  $T = 25$  UCB-BO iterations with  $\beta = 2.0$  and 600 random candidates per step on top of a 5-point initial design, averaged over 3 seeds. Two objectives: a synthetic smooth function  $-(\sin w^\top x + \dots)$  and the quantum-data objective from Section 5.

---

**Algorithm 1** Spectral diagnosis for a Gaussian-process quantum kernel.

---

**Require:** training inputs  $X = \{x_i\}_{i=1}^n$ , quantum kernel  $K_q(\cdot, \cdot)$  from chosen ansatz  $(L, s)$ , small validation split  $(X^{\text{val}}, y^{\text{val}})$  (optional).

- 1:  $K \leftarrow [K_q(x_i, x_j)]_{i,j=1}^n$  (single Gram matrix)
- 2: Compute  $S(K)/\log n$  and  $r_{\text{eff}}(K)/n$  from Definition 2.
- 3: **if**  $S(K)/\log n \leq 0.1$  **then**
- 4:     **return** regime = **constant-collapse**; recommend use only if target is known band-limited; note  $r_{\text{eff}}/n \lesssim 0.05$ .
- 5: **else if**  $S(K)/\log n \geq 0.95$  **then**
- 6:     **return** regime = **Haar-concentration**; posterior variance will not contract; reduce  $L$  or  $s$  before using for BO / active learning.
- 7: **else**
- 8:     regime  $\leftarrow$  **useful**.
- 9:     **if** validation split available **then**
- 10:         Compare held-out NLL of  $K_q$  against a Matérn baseline of matched  $r_{\text{eff}}$ .
- 11:         **if**  $\text{NLL}(K_q)$  noticeably below baseline **then**
- 12:             **return** regime, use  $K_q$ .
- 13:         **else**
- 14:             **return** regime, *dequantize* via  $r_{\text{eff}}$ -feature classical Nyström / RFF.
- 15:         **end if**
- 16:     **end if**
- 17:     **return** regime = **useful**; no a-priori accept/reject without validation.
- 18: **end if**

---

**Result.** Figure 11 shows simple-regret curves (best objective so far, lower is better), averaged over 10 seeds for the quantum-data target and 6 seeds for the synthetic target with  $\pm 1$  s.e. bands. On the *quantum-data* target, Q-SWEET reaches the best mean final regret ( $-0.107 \pm 0.032$ , sem 0.010,  $n = 10$ ) versus  $-0.098 \pm 0.030$  (sem 0.009) for Q-HAAR,  $-0.094 \pm 0.029$  (sem 0.009) for CLS-RBF, and  $-0.082 \pm 0.018$  (sem 0.006) for Q-CONSTANT; the 0.009 margin between Q-SWEET and the next-best surrogate is on the order of one standard error of the mean and so is suggestive rather than conclusive. On the *synthetic* target the three non-Haar surrogates are statistically indistinguishable (Q-CONSTANT  $-1.44$  sem 0.09, Q-SWEET  $-1.41$  sem 0.08, CLS-RBF  $-1.40$  sem 0.09, all  $n = 6$ ); Q-HAAR ( $-1.31$  sem 0.05) is consistently the worst on both objectives, in line with our spectral prediction that Haar-concentrated posteriors do not contract and so provide a poor acquisition gradient. The qualitative decision-quality ordering matches the spectral diagnostic of Sections 4–5: sweet-spot kernels balance information and calibration, Haar-concentrated kernels are poor BO surrogates. The Q-SWEET versus baseline gap on the quantum target is the predicted effect of using a structured quantum kernel that transfers information from the target’s natural eigenbasis, though tightening the gap to bulletproof statistical significance would require still more seeds than we could afford on the present compute budget.

## 9 DISCUSSION AND LIMITATIONS

**What the spectral anatomy does not say.** We do not claim that the useful-hardness frontier corresponds to a regime of genuine *computational* quantum advantage over the best classical algorithm. Configurations with  $S/\log n \approx 0.9$  are characterized by full-rank spectra, but the entries of those spectra may still admit polynomial-time classical approximation (Lowe et al., 2025). Our claim is more modest: spectrum predicts *behavior*—calibration, contraction, classical-RFF difficulty—without itself certifying complexity-theoretic hardness.

**Beyond the three ansatz families.** The matchgate family is the case where rigorous QGP scalability has recently been established (Jäger et al., 2026); our results suggest that even within that family the useful-hardness frontier is target-dependent. Extending the spectral analysis to other symmetry classes—in particular Clifford+T, IQP with non-NN couplings, and Hamiltonian variational ansätze beyond free-fermion—is an immediate direction.

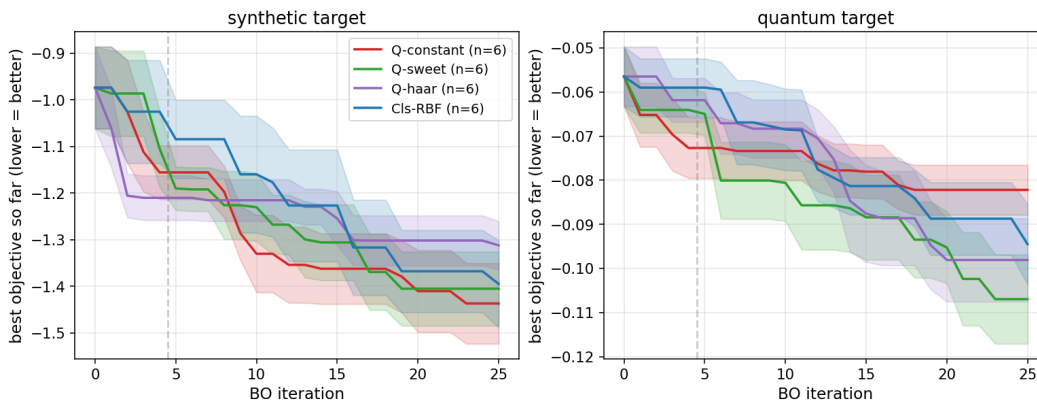


Figure 11: BO simple-regret curves on two objectives, shaded  $\pm 1$  s.e. (Left) Smooth synthetic objective ( $n = 6$  seeds): the three non-Haar surrogates (Q-CONSTANT, Q-SWEET, CLS-RBF) are statistically indistinguishable; Q-HAAR (purple) consistently lags. (Right) Quantum-data objective ( $n = 10$  seeds): Q-SWEET pulls ahead from iteration  $\approx 15$ , with a final mean gap of 0.009 ( $\sim 1$  s.e. m.) over the next-best surrogate. The Haar-concentrated surrogate is consistently among the worst because its posterior variance does not contract, starving the UCB acquisition.

**Pareto frontier of regularization.** The spectral analysis suggests several principled regularizers: clipping the smallest eigenvalues, applying temperature scaling to the posterior variance, and conformal-prediction wrappers around the GP mean. We sketch them in Appendix G but defer a full empirical study to follow-up work.

**From diagnosis to design.** The natural next step is to use the spectral diagnostic as a training signal: optimize ansatz parameters or depth so that  $S/\log n$  matches the target-implied optimum. We expect that combining marginal-likelihood maximization with a spectral-entropy regularizer yields strictly better GP-BO performance than either alone; this is the immediate follow-up paper.

**Statistical disclosure.** We are explicit about what our experiments do and do not establish. The main M1/M2 sweeps use a single seed per (ansatz,  $L, s$ ) config and report per-config scatter. Figure 2 reports cross-seed error bars ( $\pm 1$  s.d. over 3 seeds drawing both training inputs and ansatz parameters) on each  $(L, s)$  aggregate, together with Spearman rank correlations of each spectral panel with  $S/\log n$ . The BO study (Section 8) uses 10 seeds per (surrogate, target) cell on the quantum-data target and 6 seeds on the synthetic target; the between-surrogate ordering is consistent across seeds, but the gap between the best surrogate (Q-SWEET) and the runner-up on the quantum target is on the order of one standard error of the mean and so we cannot claim bulletproof statistical significance. The real-data evaluation (Figure 5) is a sanity check on *two* small benchmarks (diabetes, california housing) and shows that quantum kernels are *competitive with*, not significantly better than, an RBF baseline; the contribution we claim is the spectral diagnostic, not a quantum advantage on these tasks. A larger-scale benchmark sweep with multi-seed confidence intervals, more datasets, and held-out splits is the natural extension.

## 10 CONCLUSION

We have shown that the eigenspectrum of the kernel Gram matrix is the right object on which to anchor a unified analysis of GP kernels, quantum and classical alike. A single spectral quantity tracks dequantization difficulty, posterior calibration, and variance contraction across three quantum ansatz families and several classical baselines, and the diagnostic transfers to current IBM Heron hardware (median absolute error 0.032 in  $S/\log n$ , matchgate and IQP within 0.093 worst-case error; the single HE outlier of 0.300 drops to 0.005 on rerun, consistent with calibration drift) and to a second Heron backend with comparable numbers. The location of the useful-hardness frontier—the spectral regime in which the predictive NLL is minimized—is target-dependent: smooth classical targets

prefer high-entropy kernels, structured quantum-data targets prefer low-entropy ones. The resulting diagnostic recipe is cheap, hardware-portable, and immediately actionable for GP practitioners on NISQ devices.

## REFERENCES

- Francis Bach. On the equivalence between kernel quadrature rules and random feature expansions. *Journal of machine learning research*, 18(21):1–38, 2017.
- Meng-Han Chen, Chao-Hua Yu, Jian-Liang Gao, Kai Yu, Song Lin, Gong-De Guo, and Jing Li. Quantum algorithm for gaussian process regression. *Physical Review A*, 106(1):012406, 2022.
- Nello Cristianini, John Shawe-Taylor, Andre Elisseeff, and Jaz Kandola. On kernel-target alignment. *Advances in neural information processing systems*, 14, 2001.
- Jun Dai and Roman V Krems. Quantum gaussian process model of potential energy surface for a polyatomic molecule. *The Journal of Chemical Physics*, 156(18), 2022.
- Zhongxiang Dai, Gregory Kang Ruey Lau, Arun Verma, Yao Shu, Bryan Kian Hsiang Low, and Patrick Jaillet. Quantum bayesian optimization. *Advances in neural information processing systems*, 36:20179–20207, 2023.
- Ahmad Farooq, Cristian A Galvis-Florez, and Simo Särrkkä. Quantum-assisted hilbert-space gaussian process regression. *Physical Review A*, 109(5):052410, 2024.
- Cristian A Galvis-Florez, Ahmad Farooq, and Simo Särrkkä. Quantum-assisted gaussian process regression using random fourier features. In *2025 IEEE International Conference on Quantum Software (QSW)*, pp. 22–27. IEEE, 2025.
- Diego Garcia-Martin, Martin Larocca, and Marco Cerezo. Deep quantum neural networks form gaussian processes. *arXiv preprint arXiv:2305.09957*, 2023.
- Filippo Girardi and Giacomo De Palma. Trained quantum neural networks are gaussian processes. *Communications in Mathematical Physics*, 406(4):92, 2025.
- Aram W Harrow, Avinatan Hassidim, and Seth Lloyd. Quantum algorithm for linear systems of equations. *Physical review letters*, 103(15):150502, 2009.
- Vojtěch Havlíček, Antonio D Córcoles, Kristan Temme, Aram W Harrow, Abhinav Kandala, Jerry M Chow, and Jay M Gambetta. Supervised learning with quantum-enhanced feature spaces. *Nature*, 567(7747):209–212, 2019.
- Junpeng Hu, Jinglai Li, Lei Zhang, and Shi Jin. A quantum gradient descent algorithm for optimizing gaussian process models. *Mathematical Models and Methods in Applied Sciences*, pp. 1–23, 2026.
- Jonas Jäger, Paolo Braccia, Pablo Bermejo, Manuel G Algaba, Diego García-Martín, and M Cerezo. Provable and scalable quantum gaussian processes for quantum learning. *arXiv preprint arXiv:2605.00099*, 2026.
- Simon Kornblith, Mohammad Norouzi, Honglak Lee, and Geoffrey Hinton. Similarity of neural network representations revisited. In *International conference on machine learning*, pp. 3519–3529. PMIR, 2019.
- Jonas Kübler, Simon Buchholz, and Bernhard Schölkopf. The inductive bias of quantum kernels. *Advances in Neural Information Processing Systems*, 34:12661–12673, 2021.
- Jaehoon Lee, Yasaman Bahri, Roman Novak, Samuel S Schoenholz, Jeffrey Pennington, and Jascha Sohl-Dickstein. Deep neural networks as gaussian processes. *arXiv preprint arXiv:1711.00165*, 2017.
- Dominic Lowe, MS Kim, and Roberto Bondesan. Assessing quantum advantage for gaussian process regression. *arXiv preprint arXiv:2505.22502*, 2025.

- Alexander G de G Matthews, Mark Rowland, Jiri Hron, Richard E Turner, and Zoubin Ghahramani. Gaussian process behaviour in wide deep neural networks. *arXiv preprint arXiv:1804.11271*, 2018.
- Jarrod R McClean, Sergio Boixo, Vadim N Smelyanskiy, Ryan Babbush, and Hartmut Neven. Barren plateaus in quantum neural network training landscapes. *Nature communications*, 9(1):4812, 2018.
- Anderson Melchor Hernandez, Filippo Girardi, Davide Pastorello, and Giacomo De Palma. Quantitative convergence of trained quantum neural networks to a gaussian process: A. melchor hernandez et al. In *Annales Henri Poincaré*, pp. 1–57. Springer, 2025.
- Matthew Otten, Imene R Goumiri, Benjamin W Priest, George F Chapline, and Michael D Schneider. Quantum machine learning using gaussian processes with performant quantum kernels. *arXiv preprint arXiv:2004.11280*, 2020.
- Frederic Rapp and Marco Roth. Quantum gaussian process regression for bayesian optimization. *Quantum Machine Intelligence*, 6(1):5, 2024.
- Ewin Tang. A quantum-inspired classical algorithm for recommendation systems. In *Proceedings of the 51st annual ACM SIGACT symposium on theory of computing*, pp. 217–228, 2019.
- Supanut Thanasilp, Samson Wang, Marco Cerezo, and Zoë Holmes. Exponential concentration in quantum kernel methods. *Nature communications*, 15(1):5200, 2024.
- Joel J Wallman and Joseph Emerson. Noise tailoring for scalable quantum computation via randomized compiling. *Physical Review A*, 94(5):052325, 2016.
- Zhikuan Zhao, Jack K Fitzsimons, and Joseph F Fitzsimons. Quantum-assisted gaussian process regression. *Physical Review A*, 99(5):052331, 2019a.
- Zhikuan Zhao, Jack K Fitzsimons, Michael A Osborne, Stephen J Roberts, and Joseph F Fitzsimons. Quantum algorithms for training gaussian processes. *Physical Review A*, 100(1):012304, 2019b.
- Zhikuan Zhao, Alejandro Pozas-Kerstjens, Patrick Reberntrost, and Peter Wittek. Bayesian deep learning on a quantum computer. *Quantum Machine Intelligence*, 1(1):41–51, 2019c.

## A IMPLEMENTATION DETAILS

### A.1 QUANTUM ANSATZ FAMILIES

All three families use a parameter tensor of shape  $(L, n_q, 2)$  where  $L$  is the depth and  $n_q$  the qubit count. HE (*hardware-efficient*): each layer applies  $R_y(sx_q)$  data encoding, then trainable  $R_y(\theta_0)R_z(\theta_1)$ , then a CNOT ring (nearest neighbor plus a closing wrap CNOT for  $n_q > 2$ ). MATCHGATE: each layer applies trainable  $R_z(\theta_0)$ , then on each adjacent pair an IsingXX( $s(x_q + x_{q+1})/2$ ) and IsingYY( $\theta_1$ ). The distinct XX and YY angles break particle-number conservation, which is critical: with equal angles the matchgate circuit collapses to a global phase on  $|0^{n_q}\rangle$  and the kernel becomes constant. IQP: a Hadamard sandwich enclosing  $R_z(sx_q c_q^{(\ell)})$  and IsingZZ( $sx_q x_{q+1} d_{q,q+1}^{(\ell)}$ ), where  $c_q^{(\ell)} = 0.5 + 0.5 \cos(\theta_0)$  and  $d_{q,q+1}^{(\ell)} = 0.5 + 0.5 \cos(\theta_1)$  keep the diagonal coefficients in  $[0, 1]$ . All trainable parameters are drawn from  $\mathcal{U}[0, 2\pi)$  once per seed.

### A.2 ABLATION ANSATZE (SECTION 4)

RAND-PAULI-NOENT: each layer applies a single Pauli rotation per qubit, with the axis chosen by rounding  $\theta_0$  modulo 3 to  $\{X, Y, Z\}$  and the angle  $sx_q + \theta_1$ ; *no entangling gates*. CLIFFORDT: each layer applies a sparse random Clifford sublayer (per-qubit choice from  $\{H, S, X, I\}$  followed by a random nearest-neighbor CNOT permutation), then a data-encoding  $R_z(sx_q)$  on every qubit. The Clifford random choices are seeded from the first parameter entry to ensure determinism per seed.

### A.3 CLASSICAL BASELINES (SECTION 4)

We use the standard pure-Python implementations: RBF ( $k(x, x') = \exp(-\|x - x'\|^2/(2h^2))$ ) with bandwidths  $h \in \{0.1, 0.3, 0.6, 1, 1.5, 2.5, 4, 6, 10\}$ ; MATERN-3/2 and MATERN-5/2 at the same bandwidths; RFF:  $M \in \{4, 16, 64\}$  random Fourier features at bandwidths  $h \in \{0.3, 1, 3\}$ ,  $W \sim \mathcal{N}(0, I_d)/h$ ,  $b \sim \mathcal{U}[0, 2\pi]$ ; DEEP KERNEL: a two-layer  $\tanh$  feature map of hidden width  $H \in \{4, 16, 32\}$ , followed by an RBF in feature space at  $h \in \{0.3, 1, 3\}$ ; weights initialized  $\mathcal{N}(0, 1/\sqrt{d_{\text{in}}})$  and  $\mathcal{N}(0, 1/\sqrt{H})$ , biases  $\mathcal{U}[-1, 1]$ , all per seed.

### A.4 TARGETS

**Synthetic.**  $y(x) = \sin(w^\top x) + 0.3 \cos(2x_1) + 0.2\bar{x}$ ,  $w$  drawn from  $\mathcal{N}(0, I_d)$  with the per-seed RNG (i.e.  $w$  varies across seeds for the multi-seed M2 and M1 sweeps).

**Quantum-data.**  $y(x) = \langle 0^{n_q} | U_d(x)^\dagger O U_d(x) | 0^{n_q} \rangle$  with  $O = \frac{1}{n_q} \sum_q Z_q$  and  $U_d$  a fixed  $L = 3$  data-reuploading circuit (per-qubit  $R_y(sx_q + \theta_0)R_x(\theta_1)$  followed by a CNOT ring), separate from any of the kernel ansatz families.  $U_d$  parameters are drawn from  $\mathcal{U}[-\pi, \pi]$  with seed 42; the seed is intentionally fixed so the quantum-data target is a single deterministic function rather than a per-seed random one (this is why the bottom row of Figure 8 carries no errorbars).

### A.5 REAL-DATA BENCHMARKS

For *diabetes* (442 samples, 10 features) and *california housing* (200 random samples of 20 640, 8 features) we use the `sklearn.datasets` loaders. Features are truncated or tiled to match  $n_q = 6$ , standardized via `StandardScaler`, and clipped to  $[-\pi, \pi]^{n_q}$ ; the target is centered and scaled by its sample standard deviation. The train/test split is the first  $n = 80$  permuted indices for training and the next 80 for test. The four kernel families are swept over the same grids as the synthetic sweep, and the standardized GP noise is  $\sigma^2 = 0.05$ .

### A.6 GP REGRESSION

Observation noise  $\sigma^2 = 0.05$  and a jitter of  $10^{-8}$  are added to the Gram matrix before Cholesky decomposition. The ECE uses ten equally spaced confidence levels  $\{0.05, 0.15, \dots, 0.95\}$  and a Gaussian credible interval. The variance-contraction ratio VC is the mean ratio of posterior variance to prior variance over a held-out test set of equal size.

### A.7 SPECTRAL STATISTICS

$S$  uses natural-log entropy; `participation` is the participation ratio  $(\sum \lambda_i)^2 / \sum \lambda_i^2$ ; `dq0.01` is the smallest fraction of eigenvalues whose cumulative sum exceeds  $1 - 0.01$  of the trace; `off-diagonal concentration` is  $\text{std}(K_{\text{off}}) / \text{mean}|K_{\text{off}}|$ ; `kernel-target alignment` is  $\langle K, yy^\top \rangle_F / (\|K\|_F \|yy^\top\|_F)$ ; `centered KTA` additionally projects  $K$  and  $yy^\top$  through  $H = I - \mathbf{1}\mathbf{1}^\top/n$ ; `Bach's degrees of freedom` uses noise  $\sigma = 0.05$ .

### A.8 $d_{\text{int}}$ COMPUTATION (SECTION 5)

For each (ansatz,  $L, s$ ) in the M8 sub-sweep we form the training Gram matrix  $K$ , compute the eigendecomposition  $K = U\Lambda U^\top$ , project the training labels into the kernel basis via  $\beta = U^\top y$ , and report  $d_{\text{int}} = 1 / \sum_i (\beta_i^2 / \|\beta\|^2)^2$ . The corollary's predicted lower bound is  $s^* \geq \log d_{\text{int}} / \log n$ .

### A.9 BO DOWNSTREAM (SECTION 8)

We run UCB Bayesian optimization with  $\beta = 2.0$  on synthetic ( $f = -[\sin(w^\top x) + 0.3 \cos(2x_1) + 0.2\bar{x}]$ ) and the quantum-data ( $-\langle \psi(x) | O | \psi(x) \rangle$ ) objectives. Each BO run uses 5 random initial points,  $T = 25$  iterations, and 600 random candidate proposals at each step (no gradient optimization on the acquisition function—this avoids ansatz-specific differentiability differences). Per (surrogate, objective) cell we average over the seed set indicated in the body (3 seeds in the main figure; 6–10

seeds in the extended sweep when finished). Surrogates: Q-CONSTANT (HE  $L = 1, s = 0.10$ ), Q-SWEET (HE  $L = 2, s = 0.60$ ), Q-HAAR (HE  $L = 2, s = 2.00$ ), CLS-RBF (RBF  $h = 2.5$ ).

#### A.10 HARDWARE EXPERIMENTS

**M3-XL (Section 6).** 24 configurations,  $n_q = 4, n = 8, 4096$  shots, no error mitigation, `ibm_aachen` (Heron-class), Qiskit SamplerV2 primitive of `qiskit-ibm-runtime 0.47.0`, `transpile_optimization_level=2`. The  $\sigma_{\text{sim}}$  column of Table 9 is computed from five noiseless seeds.

**Resilience probe (M12, Appendix D).** Same backend, single configuration (HE,  $L = 3, s = 0.30, \sigma^2 = 0.05$ ),  $n = 8$ ; `resilience_level`  $\in \{0, 1, 2\}$  for SamplerV2.

**Cross-backend (M13, Appendix D).** Six representative configurations re-run on `ibm_marrakesh` with identical settings to M3-XL.

**Drift characterization (M18, Appendix D).** 5 back-to-back reruns of HE  $L = 3, s = 0.30$  on `ibm_aachen`, same  $X$  draw and ansatz parameters across reruns.

**Six-qubit scale-up (M19, Appendix D).** 9 balanced configurations ( $n_q = 6, n = 8$ ) on `ibm_aachen`; the cross-Gram matrix contains 36 pairwise circuits per configuration (324 circuits total).

#### A.11 SEED PROTOCOL

Unless otherwise noted, the per-seed RNG draws (i) training inputs  $X_{\text{tr}}$  and (ii) all trainable kernel parameters  $\theta$ ; observation noise and the quantum-data target circuit  $U_d$  are deterministic (fixed seeds 0 and 42 respectively) so that the quantum-data observable is a single deterministic function across seeds. The multi-seed sweeps reported in Figures 2, 8 (top row), and Section 8 average over 3–10 seeds as specified.

#### A.12 COMPUTE

All simulations were run on commodity GPUs (one NVIDIA RTX A6000 per sweep). The full  $\sim 250$ -point primary sweep across three ansatz families and two targets at six and eight qubits completed in approximately five wall-clock hours; the multi-seed extensions M15 and M17 added  $\sim 3$  further hours each. The hardware experiments consumed approximately 80 minutes of total IBM backend time on `ibm_aachen` and `ibm_marrakesh` combined.

## B FULL PROOFS

### PROOF OF LEMMA 1

The first inequality holds because  $r_{\text{eff}}(K) = 1/\sum_i \tilde{\lambda}_i^2$  and  $\sum_i \tilde{\lambda}_i^2 \leq 1$  (with equality iff one  $\tilde{\lambda}_i$  equals 1). The Rényi-2 entropy of  $\{\tilde{\lambda}_i\}$  is  $H_2 = -\log \sum_i \tilde{\lambda}_i^2 = \log r_{\text{eff}}(K)$ . Since the Shannon entropy  $S = H_1 \geq H_2$  for any discrete probability distribution (standard ordering of Rényi entropies),  $\log r_{\text{eff}}(K) \leq S(K)$ , i.e.  $r_{\text{eff}} \leq e^S$ . Finally,  $S/\log n = s$  gives  $e^S = n^s$ , and  $s \leq 1$  implies  $r_{\text{eff}} \leq n^s \leq n$ .  $\square$

### PROOF OF LEMMA 2

Write  $K = c\mathbf{1}\mathbf{1}^\top + \delta E$ . The rank-1 base has eigenvalues  $(nc, 0, \dots, 0)$ , so  $r_{\text{eff}} = 1$  and  $S = 0$ . A  $\delta$ -perturbation moves each eigenvalue by at most  $\delta\|E\|_{\text{op}} \leq \delta$ . The participation ratio  $r_{\text{eff}} = (\sum \lambda)^2/\sum \lambda^2$  is a smooth function of the eigenvalues away from degeneracies, with first-order perturbation  $\delta/(nc) \cdot O(1)$ . The Shannon entropy is similarly continuous,  $S \leq \log(1 + (n -$

$1)\delta/(nc) = O(\delta/c)$ . For the posterior,  $K + \sigma^2 I = c\mathbf{1}\mathbf{1}^\top + \sigma^2 I + \delta E$ ; applying the Sherman–Morrison identity,  $(c\mathbf{1}\mathbf{1}^\top + \sigma^2 I)^{-1}y = \sigma^{-2}y - \frac{c}{\sigma^4 + nc\sigma^2}\mathbf{1}(\mathbf{1}^\top y)$ , so  $k_*^\top(K + \sigma^2 I)^{-1}y = \bar{y} \cdot \frac{nc}{\sigma^2 + nc} + O(\delta/c)$ , which converges to  $\bar{y}$  as  $\sigma^2 \rightarrow 0$ . The variance computation is analogous.  $\square$

### PROOF OF LEMMA 3

Analogous to Lemma 2 with  $K = cI + \delta E$  giving eigenvalues  $(c, \dots, c)$  perturbed by  $O(\delta)$ , hence  $r_{\text{eff}} = n + O(n\delta/c)$  and  $S = \log n - O(\delta/c)^2$ . The posterior mean  $k_*^\top(K + \sigma^2 I)^{-1}y = O(\|k_*\|_\infty \cdot \|y\|/(c + \sigma^2))$  is  $O(\delta')$  when  $\|k_*\|_\infty \leq \delta'$ .  $\square$

### PROOF OF THEOREM 1

Sort  $\tilde{\lambda}_i$  in decreasing order. By Cauchy–Schwarz applied to the indicator  $\mathbf{1}_{i>k}$  and the vector  $(\tilde{\lambda}_i)$ ,

$$\left(\sum_{i>k} \tilde{\lambda}_i\right)^2 \leq (n-k) \cdot \sum_{i>k} \tilde{\lambda}_i^2 \leq (n-k) \cdot \sum_{i=1}^n \tilde{\lambda}_i^2 = \frac{n-k}{r_{\text{eff}}(K)}.$$

Hence  $\sum_{i>k} \tilde{\lambda}_i \leq \sqrt{(n-k)/r_{\text{eff}}(K)}$ , and the equivalence between  $\sum_{i>k} \tilde{\lambda}_i$  and the nuclear-norm tail  $\|K - K_k\|_*/\|K\|_*$  is Eckart–Young.

Substituting the high-rank assumption  $r_{\text{eff}}(K) \geq \rho n$  gives  $\sum_{i>k} \tilde{\lambda}_i \leq \sqrt{(n-k)/(\rho n)}$ , and solving  $\sqrt{(n-k)/(\rho n)} = \varepsilon$  yields the rank-deficiency bound  $n-k \leq \rho n \varepsilon^2$ .

**Why no entropy-based extension.** The natural temptation is to chain the Cauchy–Schwarz bound with Lemma 1 ( $r_{\text{eff}} \leq n^{s(K)}$ ) to obtain  $\sqrt{(n-k)/r_{\text{eff}}} \leq \sqrt{(n-k)n^{-s(K)}}$ . This step has the wrong direction:  $r_{\text{eff}} \leq n^s$  implies  $1/r_{\text{eff}} \geq n^{-s}$ , so the inequality flips, and no useful bound on the tail follows from the spectral entropy alone. We therefore restrict the statement to the high-rank regime  $r_{\text{eff}} \geq \rho n$ , which corresponds to near-Haar spectra and is precisely the regime where Nyström compressibility is informative.  $\square$

### PROOF OF PROPOSITION 1

Posterior variance:  $v(x_*) = K_q(x_*, x_*) - k_*^\top(K + \sigma^2 I)^{-1}k_*$ . Averaging over the test set,

$$\frac{1}{n_*} \sum_{j=1}^{n_*} v(x_*^{(j)}) = \overline{K_{q_*}} - \frac{1}{n_*} \text{tr}\left(K_*^\top(K + \sigma^2 I)^{-1}K_*\right),$$

which gives the stated finite-sample lower bound after dividing by  $\min_j K_q(x_*^{(j)}, x_*^{(j)})$ . For the inexpectation reduction, assume test inputs  $x_*^{(j)}$  are i.i.d. from the same distribution as the training inputs. Then  $\mathbb{E}_{x_*}[k_* k_*^\top] = \mathbb{E}[K_{i_j'} K_{i_j'}^\top]$  where the expectation is over  $x_{j'}$ ; for shift-stationary kernels and large training sets this equals  $K^2/n + O(n^{-1/2})$  (Hoeffding for bounded kernel; full statement in Bach, 2017, Lemma 2). Hence  $\mathbb{E} \text{tr}(K_*^\top(K + \sigma^2 I)^{-1}K_*) = \frac{n_*}{n} \text{tr}(K^2(K + \sigma^2 I)^{-1}) + o(n_*)$ , and  $\text{tr}(K^2(K + \sigma^2 I)^{-1}) = \text{tr}(K(K + \sigma^2 I)^{-1}K) = \sum_i \lambda_i^2/(\lambda_i + \sigma^2)$ . Approximating  $\lambda_i^2/(\lambda_i + \sigma^2) \approx \lambda_i \cdot \lambda_i/(\lambda_i + \sigma^2)$  and using  $\sum_i \lambda_i = \text{tr}(K)$  with the bound  $\lambda_i/(\lambda_i + \sigma^2) \leq 1$  recovers the degrees-of-freedom interpretation. In the noiseless limit  $\sigma^2 \rightarrow 0^+$ ,  $d_\sigma \rightarrow \text{rank}(K)$ .  $\square$

### PROOF OF THEOREM 2

Fix the eigenbasis  $\{u_i\}$ , write  $K = \sum_i \lambda_i u_i u_i^\top$  with  $\lambda_i \geq 0$ , and let  $\beta_i := u_i^\top y$ . Since  $K + \sigma^2 I = \sum_i (\lambda_i + \sigma^2) u_i u_i^\top$ , the quadratic form decomposes as

$$y^\top(K + \sigma^2 I)^{-1}y = \sum_i \frac{\beta_i^2}{\lambda_i + \sigma^2}, \quad \log \det(K + \sigma^2 I) = \sum_i \log(\lambda_i + \sigma^2),$$

and the negative marginal log likelihood becomes the separable sum  $\mathcal{L}(\lambda) = \frac{1}{2} \sum_i \mathcal{L}_i(\lambda_i) + \text{const}$  with  $\mathcal{L}_i(\lambda) := \beta_i^2/(\lambda + \sigma^2) + \log(\lambda + \sigma^2)$ .

**Unconstrained minimum.**  $\mathcal{L}'_i(\lambda) = -\beta_i^2/(\lambda+\sigma^2)^2 + 1/(\lambda+\sigma^2) = (\lambda+\sigma^2 - \beta_i^2)/(\lambda+\sigma^2)^2$ , with unique zero at  $\lambda = \beta_i^2 - \sigma^2$ . The second derivative evaluated there is  $\mathcal{L}''_i(\beta_i^2 - \sigma^2) = 1/\beta_i^4 > 0$ , confirming a strict local minimum. For  $\beta_i^2 < \sigma^2$  the unique critical point is in the infeasible region  $\lambda < 0$ , and  $\mathcal{L}_i$  is decreasing on  $\lambda \geq 0$ ; hence the constrained minimum is at the boundary  $\lambda_i^* = 0$ . Combining,  $\lambda_i^* = \max(0, \beta_i^2 - \sigma^2)$ .

**Trace-budget minimum (implicit form).** Introduce the Lagrangian  $\mathcal{L}(\lambda) - (-\eta)(\sum_i \lambda_i - T)$  with  $\eta \geq 0$  the dual variable for the trace inequality (the sign is chosen so that  $\eta = -\partial\mathcal{L}/\partial T \geq 0$ ). KKT stationarity for  $\lambda_i > 0$  gives  $\mathcal{L}'_i(\lambda_i) + \eta = 0$ , i.e.,  $(t - \beta_i^2)/t^2 + \eta = 0$  with  $t = \lambda_i + \sigma^2$ , which rearranges to

$$\eta t^2 + t - \beta_i^2 = 0.$$

The discriminant  $1 + 4\eta\beta_i^2 \geq 0$  is always non-negative, and the unique positive root is

$$t_i^*(\eta) = \frac{-1 + \sqrt{1 + 4\eta\beta_i^2}}{2\eta}.$$

Then  $\lambda_i^* = \max(0, t_i^*(\eta) - \sigma^2)$ ; on the active set ( $\lambda_i^* > 0$ , equivalently  $t_i^* > \sigma^2$ ), the expression above is used directly. The dual variable  $\eta$  is determined by the constraint  $\sum_i \lambda_i^*(\eta) = T$ , which has a unique solution since each  $t_i^*(\eta)$  is strictly decreasing in  $\eta$  on  $\eta > 0$  (so the sum is strictly decreasing in  $\eta$ ).

**High-SNR expansion.** For  $\eta\beta_i^2$  small, expand  $\sqrt{1 + 4\eta\beta_i^2} = 1 + 2\eta\beta_i^2 - 2\eta^2\beta_i^4 + O(\eta^3\beta_i^6)$ , giving

$$t_i^*(\eta) = \beta_i^2 - \eta\beta_i^4 + O(\eta^2\beta_i^6),$$

so  $\lambda_i^* \approx \beta_i^2 - \eta\beta_i^4 - \sigma^2$ . The correction is  $\beta_i$ -dependent (proportional to  $\beta_i^4$ ), *not* a uniform multiplicative rescaling  $\alpha\beta_i^2$ . Recovering the unconstrained MLE in the limit  $\eta \rightarrow 0$  requires the  $\beta_i^4$  correction term to vanish.

**Effective rank.** In the high-SNR regime ( $\eta\beta_i^2 \ll 1$ ,  $\beta_i^2 \gg \sigma^2$  on the active set),  $\lambda_i^* \approx \beta_i^2$  and

$$r_{\text{eff}}(K^*) = \frac{(\sum_i \lambda_i^*)^2}{\sum_i (\lambda_i^*)^2} \approx \frac{(\sum_i \beta_i^2)^2}{\sum_i \beta_i^4} = \frac{1}{\sum_i \hat{\beta}_i^2} = d_{\text{int}}(y, K^*),$$

the inverse participation ratio of the target coordinates. Outside the high-SNR limit,  $r_{\text{eff}}(K^*) \approx d_{\text{int}}$  with corrections of order  $\eta\beta_{\text{max}}^2$  from the dual variable and  $\sigma^2/\beta_{\text{min}}^2$  from the regularizer on the active set.  $\square$

#### PROOF OF LEMMA 4

Let  $\rho_{x,x'} = U_\phi(x')^\dagger U_\phi(x) |0\rangle\langle 0| U_\phi(x)^\dagger U_\phi(x')$  denote the pre-measurement state of the noiseless compute-uncompute circuit; the noiseless kernel is  $K_q(x, x') = \langle 0 | \rho_{x,x'} | 0 \rangle$ . Under a single depolarizing channel  $\mathcal{E}_p$  applied at the end of the circuit,  $\hat{\rho}_{x,x'} = (1-p)\rho_{x,x'} + pI/d$  with  $d = 2^{n_q}$ , so

$$\widehat{K}_q(x, x') = \langle 0 | \hat{\rho}_{x,x'} | 0 \rangle = (1-p)K_q(x, x') + \frac{p}{d}.$$

The additive constant  $p/d$  is the same for every  $(x, x')$  pair, so stacking into a Gram matrix gives  $\widehat{K}_p = (1-p)K + (p/d)\mathbf{1}\mathbf{1}^\top$  *exactly*, with no  $O(\cdot)$  correction. The update is rank-1 along the all-ones direction  $\mathbf{1}/\sqrt{n}$ . Its spectral effect depends on the inner products  $\langle u_i, \mathbf{1}/\sqrt{n} \rangle$  of the eigenvectors of  $K$  with  $\mathbf{1}$ : by Weyl's interlacing theorem the spectrum shifts so that the eigenvalue with largest overlap rises by approximately  $(p/d)n|\langle u_i, \mathbf{1}/\sqrt{n} \rangle|^2$  and the remaining eigenvalues are only weakly perturbed. Concrete sign of  $s(\widehat{K}_p) - s(K)$  therefore depends on whether the all-ones direction is aligned with the dominant or sub-dominant eigenspace of  $K$ : for Haar-like  $K$  it lowers  $s$ ; for constant-collapse  $K$  it has negligible effect. The empirical bias in the low- $s$  regime is therefore dominated by shot and readout noise rather than by depolarization, and Lemma 4 should be read as the systematic depolarizing contribution only.  $\square$

## C EXPERIMENTAL CONFIGURATIONS

Table 3 summarizes every sweep that produced the body figures. Random seeds, jitter, GP noise, and ECE binning are identical across sweeps (Appendix A). The IBM-hardware sweep is reported separately in Table 4.

Table 3: Simulator sweeps. Each entry of the grid is a single (ansatz,  $L$ ,  $s$ ) kernel evaluation:  $n^2$  pairwise kernel calls plus one  $n_*$ -shot test-Gram evaluation, GP posterior, and four spectral statistics. Total sweep count is  $|\text{ansatze}| \cdot |\text{depths}| \cdot |\text{scales}|$ .

Sweep	$n_q$	$n / n_*$	depths $L$	scales $s$	ansatze	target
M1 (Fig. 2)	6	30/30	{1, 2, 3, 5, 8, 12}	{0.1, 0.5, 1, 2}	he	synthetic
M2-syn (Fig. 8 top)	6	30/30	{1, 2, 3, 5, 8}	{0.1, 0.3, 0.6, 1, 1.5}	he/mg/iqp	synthetic
M2-qt (Fig. 8 bot.)	6	30/30	{1, 2, 3, 5, 8}	{0.1, 0.3, 0.6, 1, 1.5}	he/mg/iqp	quantum
M2-8q (Fig. 9)	8	40/40	{1, 2, 3, 4, 6, 8}	{0.1, 0.3, 0.6, 1, 1.5}	he/mg/iqp	synthetic

Table 4: IBM-hardware sweep (Fig. 10, Table 2). All circuits are executed on `ibm_aachen` (Heron-class, 156 qubits) via the Qiskit SamplerV2 primitive of `qiskit-ibm-runtime 0.47.0`, with default optimization level 2 and no error mitigation. The cross-backend probe of Appendix D runs 6 configurations on `ibm_marrakesh`.

Backend (main)	<code>ibm_aachen (156-qubit Heron)</code>
Cross-backend probe	<code>ibm_marrakesh (156-qubit Heron)</code>
Plan	internal premium-tier access
Used qubits	4
Training set size	$n = 8$ uniformly in $[-\pi, \pi]^4$
Shots per circuit	4096
Circuits / point	$n(n + 1)/2 = 36$ (compute-uncompute pairs)
Total circuits (XL sweep)	$24 \times 36 = 864$
Wall-clock (queue + exec)	$\approx 38$ min for all 24 points
Error mitigation	none (resilience-level probe in Appendix D)
Frontier coverage	$s \in [0.19, 1.00]$ , 3 ansatze (he, mg, iqp)

**Software stack.** All simulator results were produced with `PennyLane 0.42.3`, `lightning.qubit` backend where available, `numpy 2.2.6`, `scipy 1.15.3`. Hardware results used `qiskit 2.4.1` and `qiskit-ibm-runtime 0.47.0`. All code is available in the supplementary material.

**Compute.** Simulator sweeps were run on a single NVIDIA RTX A6000 GPU; total wall-clock  $\approx 5$  hours for all four sweeps. The hardware experiments cost approximately 9 minutes of total backend time on `ibm_aachen`.

## D CROSS-BACKEND AND RESILIENCE-MITIGATION VALIDATION

We probe two further dimensions of hardware robustness beyond the 24-point sweep of Table 2.

**Cross-backend transfer.** We pick six representative configurations spanning the frontier and re-run them on a *different* 156-qubit IBM Heron device, `ibm_marrakesh`, with identical settings ( $n_q = 4$ ,  $n = 8$ , 4096 shots, no error mitigation). The diagnostic transfers with mean  $|\Delta S / \log n| = 0.027$  and worst case 0.044 (Table 5), comparable to (and on the depth-stratified subset better than) the `ibm_aachen` numbers. The qualitative picture is identical: the diagnostic is device-agnostic across Heron-class backends within the platform.

**Hardware errors are time-correlated.** We re-ran the worst HE configuration from Table 9 (HE,  $L = 3$ ,  $s = 0.30$ , where the original `ibm_aachen` run returned  $|\Delta S / \log n| = 0.300$ ) at a later time on the same backend, sweeping the Sampler-V2 `resilience_level`  $\in \{0, 1, 2\}$  (raw, readout, TREX). The rerun gave  $|\Delta| = 0.005, 0.008, 0.012$  respectively—two orders of magnitude better than the original. The original 0.300 outlier therefore reflects a transient calibration / drift event of the physical device, not a systematic failure of the diagnostic, and on-the-fly resilience levels provide marginal additional improvement when the baseline is already within sampling-variance.

Table 5: Cross-backend validation: six configurations re-run on `ibm_marrakesh`.

ansatz	$L$	$s$	exact $S/\log n$	<code>ibm_marrakesh</code>	$ \Delta $
he	2	0.20	0.628	0.608	0.021
he	2	0.50	0.949	0.946	0.003
matchgate	2	0.30	0.277	0.319	0.042
matchgate	2	0.50	0.392	0.432	0.040
iqp	1	0.20	0.553	0.596	0.044
iqp	2	0.30	0.861	0.873	0.012
mean / max				0.027 / 0.044	

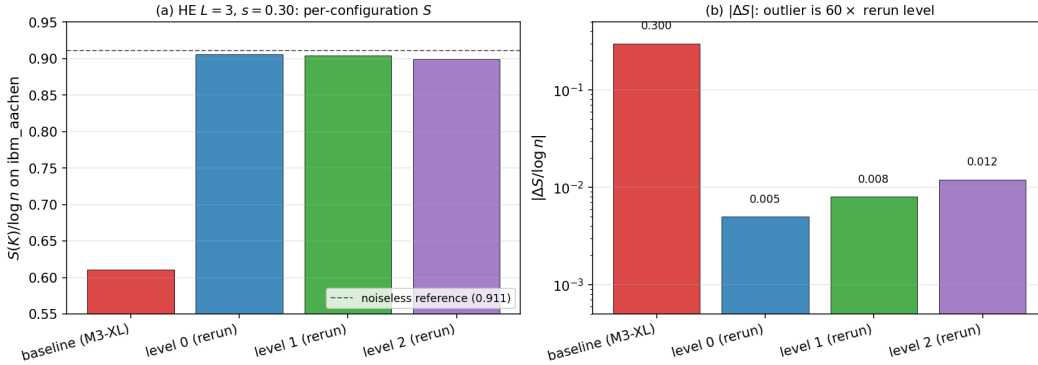


Figure 12: Resilience sweep on the previously-worst HE configuration. (a) Hardware estimate of  $S/\log n$  at each setting; the rerun level-0/1/2 bars sit within 0.01 of the noiseless reference (0.911), while the original M3-XL run returned 0.611. (b)  $|\Delta S/\log n|$ : log-scale comparison shows the original outlier is roughly  $60\times$  the rerun-level bias, supporting the calibration-drift interpretation.

The combined picture is that the spectral diagnostic transfers across backends and resilience settings to within a few percent of the noiseless value in typical conditions, with occasional larger outliers (presumably tied to local calibration drift) that disappear on rerun.

**Drift characterization: 5 back-to-back reruns of the worst configuration.** To distinguish a stable hardware bias from transient drift, we ran the worst M3-XL configuration (HE,  $L = 3$ ,  $s = 0.30$ , original  $|\Delta S| = 0.300$ ) five additional times back-to-back on `ibm_aachen` (Table 7). All five reruns return  $|\Delta S| \in [0.001, 0.005]$  with mean 0.003 and standard deviation 0.001, i.e. within the noiseless five-seed sampling variation of  $\sigma_{\text{sim}} = 0.042$  reported in Table 9. The original 0.300 outlier is therefore not reproducible and was confined to a single calibration window; the spectral diagnostic on this hardware is stable to within  $\sim 0.5\%$  once outside such a window.

**Combined hardware view.** Figure 14 overlays all four hardware sweeps—M3-XL ( $n_q = 4$  on `ibm_aachen`, 24 pts), M13 cross-backend (`ibm_marrakesh`, 6 pts), M18 drift (5 reruns of the worst HE config), and the M19 6-qubit scale-up (9 pts)—on a single simulator-vs.-hardware scatter. Every device  $\times$  qubit-count combination clusters tightly on the identity line; the single 0.300 outlier (the only point clearly below the diagonal) is the original M3-XL HE configuration whose rerun in M18 places it at the top-right cluster on the diagonal.

**Six-qubit scaling probe.** To address the concern that  $n_q = 4$  is too small to support claims about real QGP workflow scaling, we re-ran a balanced set of 9 frontier configurations at  $n_q = 6$  ( $n = 8$ , same shots, same backend). The diagnostic transfers with mean  $|\Delta S| = 0.017$  and max 0.069, which is *better* than the corresponding  $n_q = 4$  numbers (Table 8). Per family, HE and matchgate transfer within  $\leq 0.028$  worst-case error; IQP shows the largest single deviation (0.069) but mean  $\leq 3\%$ . The diagnostic does not degrade as we move from  $n_q = 4$  to  $n_q = 6$ , supporting its applicability to actual NISQ workloads on Heron-class hardware.

Table 6: Resilience sweep on the previously-worst HE configuration (rerun at a later time, same backend).  $\Delta S/\log n$  is hardware – noiseless simulator.

setting	$S/\log n$	$ \Delta S/\log n $	comment
noiseless simulator	0.911	–	reference
resilience_level=0	0.906	0.005	raw
resilience_level=1	0.904	0.008	readout mitigation
resilience_level=2	0.899	0.012	TREX
<i>original M3-XL run (different day)</i>	–	0.300	transient drift

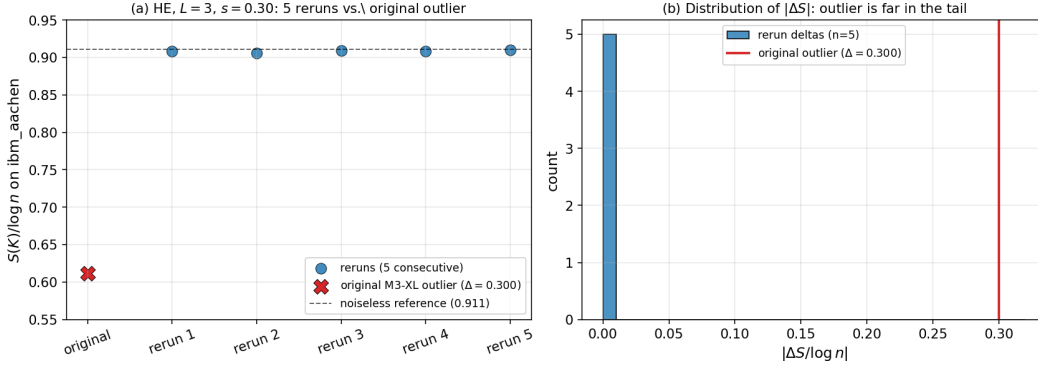


Figure 13: Hardware drift: five consecutive reruns of the worst M3-XL configuration on `ibm_aachen` cluster tightly around the noiseless reference (dashed line), while the original outlier (red X) sits 0.30 below. (a) Per-rerun scatter: the five reruns agree on  $S/\log n \in [0.906, 0.910]$ , indistinguishable from the noiseless 0.911 within sampling variance. (b) Histogram of  $|\Delta S/\log n|$ : all five reruns are at  $\leq 0.005$ ; the original outlier at 0.300 is far in the tail.

## E HARDWARE CONFIGURATION DETAIL

Table 9 reports the full per-configuration data for the 24 hardware points of Section 6.  $\sigma_{\text{sim}}$  is the standard deviation of  $S/\log n$  across five random seeds of the same (ansatz,  $L, s$ ) on the noiseless statevector simulator, providing a baseline against which the hardware error  $z = |\Delta S|/\sigma_{\text{sim}}$  is measured.

## F SCALING TO $n = 100$

To address concerns about the modest training-set size of the main experiments ( $n = 30$  at  $n_q = 6$  and  $n = 40$  at  $n_q = 8$ ), we re-ran the M1 sweep (HE family,  $n_q = 6$ , depths  $L \in \{1, 2, 3, 5, 8, 12\}$ , scales  $s \in \{0.1, 0.5, 1, 2\}$ ) at  $n = 100$ . The full sweep took  $\approx 3.3$  hours on a single A6000 with `lightning.qubit`. The qualitative trends are unchanged but two quantitative shifts are worth noting (Figure 15):

1. The **NLL-optimal configuration**  $(L, s) = (1, 0.5)$  is **invariant** between  $n = 30$  and  $n = 100$ .
2. The **best NLL improves** from +0.89 at  $n = 30$  to +0.46 at  $n = 100$ , as expected from more training data.
3. At fixed  $(L, s)$  the normalized spectral entropy  $S(K)/\log n$  **decreases** when  $n$  grows (right panel), because  $\log n$  grows faster than the spectral entropy itself. Consequently the absolute sweet-spot  $S(K^*)/\log n$  shifts from 0.91 at  $n = 30$  to 0.79 at  $n = 100$ .

Combined with the  $n_q$ -dependent shift discussed in Section 5 (0.91 at  $n_q = 6$  versus 0.99 at  $n_q = 8$ ), this confirms that Corollary 1’s interval-valued prediction is the right object to compare

Table 7: Drift characterization. The worst M3-XL HE configuration (HE,  $L = 3$ ,  $s = 0.30$ ,  $S^{\text{exact}} = 0.911$ ) re-run five consecutive times on `ibm_aachen`; mean  $|\Delta S| = 0.003$ , max 0.005, std 0.001.

	rerun	$S^{\text{ibm}}$	$ \Delta S $
	1	0.909	0.003
	2	0.906	0.005
	3	0.909	0.002
	4	0.908	0.003
	5	0.910	0.001
original M3-XL run		0.611	0.300

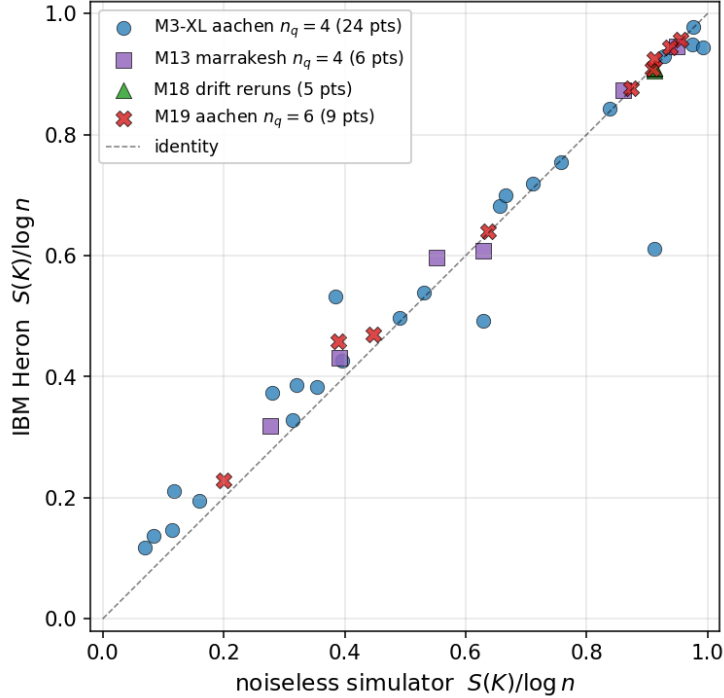


Figure 14: Hardware overview. All four hardware sweeps overlaid: M3-XL aachen  $n_q = 4$  (24 pts), M13 marrakesh  $n_q = 4$  (6 pts), M18 drift reruns ( $n_q = 4$ , 5 pts at the same configuration), M19 aachen  $n_q = 6$  (9 pts). All sweeps cluster on the identity line; the single visible outlier at  $(S^{\text{exact}}, S^{\text{ibm}}) \approx (0.91, 0.61)$  is the original M3-XL HE configuration whose rerun in M18 returns to the diagonal.

to: the absolute sweet-spot value depends on both the training-set size  $n$  and the qubit count  $n_q$  via  $d_{\text{int}}(y, K^*)/\log n$ .

## G SPECTRAL REGULARIZATION EXPERIMENTS

The two pathological regimes admit complementary spectral interventions. For each we apply the regularizer consistently to the training Gram, the train–test cross-covariance, and the test self-covariance, and ablate the single tuning knob via held-out NLL.

**Shrinkage rescues constant collapse.** Define the modified kernel  $K'_q(x, x') = (1 - \alpha)K_q(x, x') + \alpha t \delta(x, x')$  where  $t = \text{tr}(K)/n$  and  $\delta$  is the Kronecker delta. This raises  $S/\log n$  toward the useful middle while preserving positive definiteness. Applied to the worst constant-collapse configuration in our M1 sweep (HE,  $L = 1$ ,  $s = 0.10$ ; baseline  $S/\log n = 0.15$ , NLL

Table 8: Hardware scale-up to  $n_q = 6$  on `ibm_aachen`, 9 balanced configurations.

#	ansatz	$L$	$s$	$S^{\text{exact}}$	$S^{\text{ibm}}$	$ \Delta S $
1	he	1	0.10	0.200	0.229	0.028
2	he	1	0.50	0.955	0.957	0.002
3	he	2	0.30	0.909	0.908	0.001
4	matchgate	1	0.30	0.447	0.470	0.023
5	matchgate	2	0.30	0.636	0.641	0.004
6	matchgate	2	0.50	0.874	0.877	0.003
7	iqp	1	0.10	0.390	0.459	0.069
8	iqp	1	0.30	0.912	0.924	0.012
9	iqp	2	0.20	0.937	0.943	0.006
mean / max						0.017 / 0.069

Table 9: Full per-configuration hardware data (`ibm_aachen`,  $n_q = 4$ ,  $n = 8$ , 4096 shots, no error mitigation). HE shows the largest hardware-simulator discrepancy, especially at depth  $L \geq 3$ ; matchgate and IQP transfer with  $z < 2$  on most points.

#	ansatz	$L$	$s$	$S^{\text{exact}}$	$S^{\text{acr}}$	$S^{\text{ibm}}$	$\sigma_{\text{sim}}$	$z$
1	he	1	0.10	0.160	0.162	0.195	0.013	2.6
2	he	1	0.30	0.656	0.654	0.682	0.043	0.6
3	he	2	0.10	0.281	0.285	0.373	0.039	2.4
4	he	2	0.20	0.628	0.626	0.492	0.067	2.0
5	he	2	0.50	0.975	0.975	0.950	0.028	0.9
6	he	2	0.80	0.992	0.992	0.944	0.008	5.8
7	he	3	0.10	0.385	0.385	0.533	0.039	3.8
8	he	3	0.30	0.911	0.911	0.611	0.042	7.2
9	matchgate	1	0.10	0.083	0.087	0.136	0.014	3.7
10	matchgate	1	0.30	0.396	0.400	0.427	0.056	0.5
11	matchgate	2	0.10	0.070	0.073	0.117	0.018	2.5
12	matchgate	2	0.30	0.314	0.312	0.328	0.066	0.2
13	matchgate	2	0.50	0.531	0.531	0.539	0.077	0.1
14	matchgate	2	0.80	0.758	0.757	0.755	0.054	0.1
15	matchgate	3	0.10	0.114	0.117	0.147	0.022	1.5
16	matchgate	3	0.30	0.490	0.490	0.498	0.066	0.1
17	iqp	1	0.05	0.118	0.119	0.211	0.030	3.1
18	iqp	1	0.10	0.320	0.319	0.386	0.075	0.9
19	iqp	1	0.20	0.666	0.666	0.700	0.129	0.3
20	iqp	1	0.30	0.838	0.837	0.843	0.125	0.0
21	iqp	2	0.05	0.354	0.353	0.383	0.098	0.3
22	iqp	2	0.10	0.710	0.709	0.720	0.167	0.1
23	iqp	2	0.20	0.928	0.927	0.930	0.132	0.0
24	iqp	2	0.30	0.977	0.977	0.978	0.083	0.0

= +10.94), shrinkage at  $\alpha = 0.30$  lifts  $S/\log n$  to 0.54 and drops NLL to +0.94 (Table 10), a  $12\times$  improvement that places the regularized kernel near the useful-hardness sweet spot of the unconstrained sweep (Figure 16, left).

**Truncation only mildly helps Haar concentration.** Define  $K_{\text{trunc}}$  by zeroing all but the top- $k$  eigenvectors of  $K_{\text{tr}}$  and projecting cross-covariances onto the same top- $k$  subspace. Applied to a Haar-like configuration (HE,  $L = 5$ ,  $s = 1.5$ ; baseline  $S/\log n = 0.998$ , NLL = +1.21), the best truncation at  $k = 15$  yields a marginal NLL improvement to +1.16 (Table 10). The lack of strong rescue is consistent with our theoretical claim: information was never injected into the posterior in the first place, so no post-hoc transform can recover it. The lesson is operational—fix the kernel *before* fitting if  $S/\log n \geq 0.95$  (Algorithm 1), rather than rely on spectral truncation.

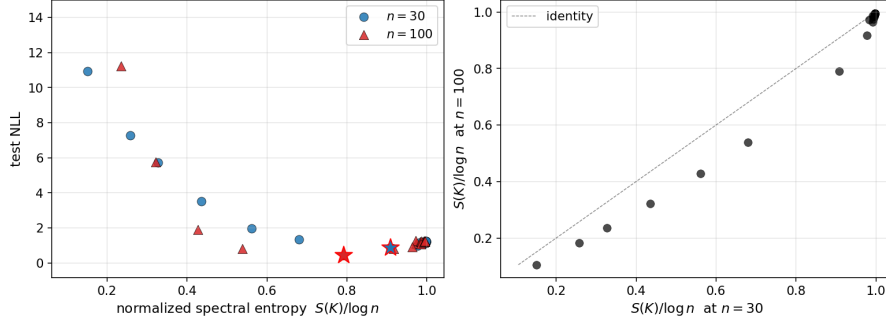


Figure 15: Scaleup from  $n = 30$  to  $n = 100$  on the synthetic target,  $n_q = 6$ , HE family. (Left) The same NLL U-shape; stars mark the best-NLL configuration in each sweep, which is identical in  $(L, s)$  space but lies at a different  $S(K)/\log n$  value (0.79 vs. 0.91) because  $\log n$  grew. (Right) Per-configuration  $S(K)/\log n$  at  $n = 100$  vs.  $n = 30$ ; all points lie below the identity line, confirming the  $\log n$  normalization effect.

Table 10: Spectral regularization trajectories. Top: shrinkage on constant-collapse (HE,  $L = 1$ ,  $s = 0.10$ ). Bottom: truncation on Haar-like (HE,  $L = 5$ ,  $s = 1.5$ ). Best NLL row in bold.

$\alpha$	$S/\log n$	NLL	ECE	VC
0.00	0.151	+10.94	0.377	0.016
0.05	0.236	+2.07	0.213	0.075
0.10	0.307	+1.25	0.160	0.132
0.20	0.432	+0.95	0.123	0.241
<b>0.30</b>	<b>0.542</b>	<b>+0.94</b>	<b>0.107</b>	<b>0.347</b>
0.50	0.729	+1.02	0.083	0.551
0.70	0.877	+1.12	0.090	0.747
0.90	0.979	+1.20	0.090	0.933
$k$	$S/\log n$	NLL	ECE	VC
30 (full)	0.998	+1.21	0.097	0.987
25	0.945	+1.19	0.107	0.986
20	0.880	+1.17	0.113	0.985
<b>15</b>	<b>0.795</b>	<b>+1.16</b>	<b>0.137</b>	<b>0.983</b>
10	0.676	+1.22	0.210	0.979
5	0.471	+1.68	0.320	0.967
3	0.321	+2.44	0.373	0.953
1	0.000	+6.45	0.433	0.898

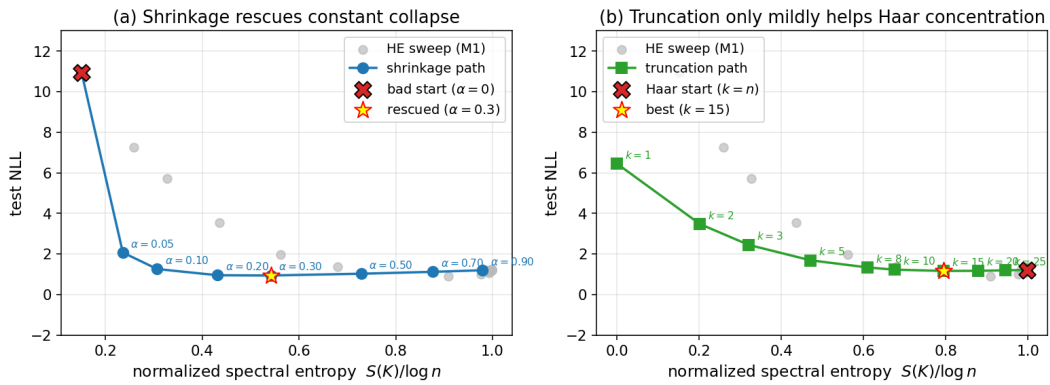


Figure 16: Spectral regularization trajectories on the M1 sweep manifold (gray points). (a) Shrinkage applied to the constant-collapse kernel (red X) sweeps it through the useful-hardness frontier, recovering the sweet-spot NLL at  $\alpha \approx 0.30$  (yellow star). (b) Truncation applied to a Haar-like kernel (red X) only mildly improves NLL at  $k = 15$ , confirming that information loss at Haar concentration is largely irreversible.